Hindawi
Journal of Nanomaterials
Volume 2023, Article ID 3555763, 22 pages
https://doi.org/10.1155/2023/3555763

Research Article

Porous Stainless Steel Microsphere Synthesis by a Nonconventional Powder Metallurgy Process Useful in the Cermet-Type Advanced Nuclear Fuel Fabrication

Luciana Sampaio Ribeiro, Francisco Javier Rios, and Armindo Santos

Centro de Desenvolvimento da Tecnologia Nuclear (CDTN/CNEN), Belo Horizonte 31270-901, MG, Brazil

Correspondence should be addressed to Armindo Santos; santosa@cdtn.br

Received 24 October 2022; Revised 15 March 2023; Accepted 25 March 2023; Published 29 April 2023

Academic Editor: Wenhui Zeng

The fabrication of SS (stainless steel)-UO_2 cermet-type advanced nuclear fuel pellets suitable for use in power reactors depends on the development of metallic (SS), ceramic (UO_2), and cermet (SS-UO_2) microspheres with special characteristics. In this work, a nonconventional powder metallurgy process was developed to produce porous SS microspheres aiming to contribute to solve the bottlenecks found in the SS-UO_2 cermet pellet manufacturing. SS, UO_2, and SS-UO_2 microspheres and SS-UO_2 cermet pellets were fabricated and characterized (XRD, EDX, EDS, and SEM). Hard ($153 \pm 5\,\mu$m; 132.2 ± 24.7 MPa; 72% TD) and soft ($216 \pm 10\,\mu$m; 1.3 ± 0.4 MPa; 17% TD) SS, hard ($176 \pm 6\,\mu$m; 147.4 ± 25.0 MPa; 99% TD) UO_2, and cermet (SS-UO_2) microspheres were obtained. The soft porous SS microspheres did not micronize properly *in situ*, but their high compressibility favors the compaction of the green SS-UO_2 cermet pellet; in this pellet, the UO_2 microspheres behaved as rigid inclusions. This favored the obtainment of sintered SS-UO_2 cermet pellets with high geometric densities (93% TD), excellent metal–ceramic interaction, and the preservation of the physical integrity of the UO_2 microspheres. The usage of high fractions of the SS-UO_2 cermet microspheres obtained mixed with low fractions of the said soft porous SS microspheres is already under development. This will enable the fabrication of SS-UO_2 cermet pellets with a volume fraction greater than 42 vol% UO_2, a homogeneous distribution of UO_2 microspheres in the metallic matrix, and null connection between them. The oxide–metal reduction mechanisms were discussed. The applicability of the process is already being explored in the manufacture of porous NdFeB microspheres.

1. Introduction

It is increasingly noted that the associated usage of nuclear and renewable source of energy can provide the energy security so necessary for the sustainable development of countries, as long as the development of new materials capable of withstanding the harsh environment of the reactor core is promoted. This harsh environment arises from the combination of high doses of neutrons, high temperatures, and a very corrosive environment. The development of these new materials has been pursued through the investigation of advanced concepts for nuclear fuels (for instance, UO_2-containing cermet fuel) and/or nuclear reactors [1–3]. In the case of advanced nuclear fuels, solutions are sought to some of the inconveniences of the oxide fuel (UO_2) currently used, namely insufficient thermal conductivity, insufficient compatibility with sodium, high release of fission gases, and heavy atom low density [2–7]. Mishra et al. [7] stated that mainly the SS matrix and, to a lesser extent, refractory metal matrix have been used in UO_2-containing cermet fuel. From a neutronic point of view, regarding the thermal neutron absorption cross-section, for example, some of the most interesting matrices for fast reactor cermet fuels are SS and molybdenum, and, for thermal reactors, zirconium or zircalloy [6, 8].

Whatever the metallic matrix, Holden [9] emphasizes that the usage of monodisperse spherical particles, both metallic and ceramic, with diameters of ~200 μm, could maximize the nuclear fuel volumetric fraction of the cermet obtained, as well as solve other bottlenecks related to null UO_2 particle interconnection, metal–ceramic interaction excellence, composite high density, and adequate containment of fission

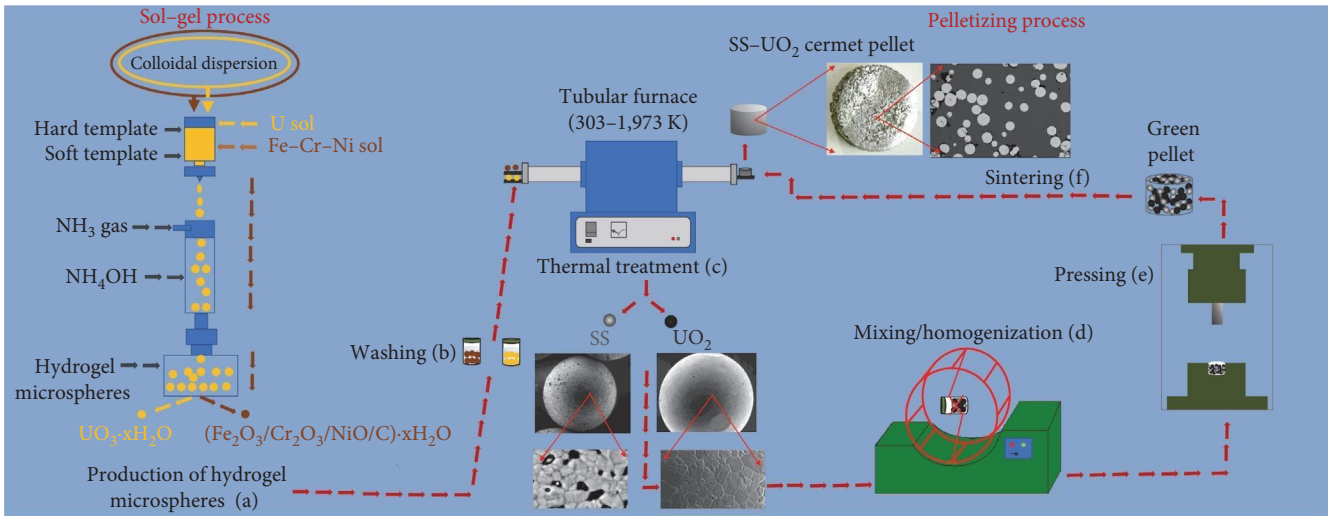

FIGURE 1: Graphical abstract of the nonconventional powder metallurgy process used in the fabrication of both SS and UO_2 microspheres and cermet (SS-UO_2) and SS pellets.

products by the metallic matrix around the UO_2 microspheres, if the physical integrity of these microspheres is preserved. However, it was impossible to verify the property of Holden's postulate [9], due to the difficulty in obtaining both soft and hard monodisperse metallic microspheres [10, 11]. In the case of metallic microspheres, there is still no well-established production process that yields characteristics appropriate for their use in the manufacture of the cermet-type nuclear fuels [4, 5, 12–14] and in other important industrial applications, such as the fabrication of both nuclear thermal propulsion fuel [8, 12] and nanostructured magnetic materials for the production of rare earth magnets [15].

SS particles with limited particle size, size distribution, shape, and density are manufactured by water atomization, gas atomization, and centrifugal atomization (or hybrid gas–water atomization) processes [16–19]. Soft and hard monodisperse UO_2 microspheres can be obtained by the sol–gel process [5, 14, 20]. Thus, the manufacture of metallic and ceramic microspheres in this R&D seeks to contribute to the development of the fabrication process of an advanced nuclear fuel represented by the dispersion of UO_2 in a stainless steel (SS) matrix. A nonconventional powder metallurgy process was used here to produce porous SS and dense UO_2 microspheres. This process results from the combination of the sol–gel method principles [5, 14, 20–22] and those of the template-assisted method in order to obtain nanostructured materials precursors of these referred microspheres [23–25]. Therefore, the focus of this work is to obtain porous SS and dense UO_2 microspheres and evaluate the pressing and sintering behaviors of these microspheres in the manufacture of SS-UO_2 cermet pellets.

2. Materials and Methods

2.1. Materials. The following analytical grade purity reagents were used without further purification: $Fe(NO_3)_3{\cdot}9H_2O$; $Cr(NO_3)_3{\cdot}9H_2O$; $Ni(NO_3)_2{\cdot}6H_2O$; $UO_2(NO_3)_2{\cdot}6H_2O$; NH_4NO_3; CH_4N_2O (urea); carbon black; $(CH_2CH(OH))_n$ (mowiol-type polyvinyl alcohol (PVA), 56–98 e $89{,}000 < Mw < 98{,}000$. Numbers 56–98 refer to two favorable characteristics for the production of SS and UO_2 microspheres: viscosity and hydrolysis. The value of 56 is associated with a viscosity of 0.056 Pa·s, obtained in a solution containing 4% PVA in water; 98 indicates the degree of hydrolysis of PVA (98.5 ± 0.5 mol%). The value range $89{,}000 < Mw < 98{,}000$ represents relatively high molecular weight values that favor obtaining a hydrogel with good resistance to elastic deformation when subjected to tensile or compressive efforts. The combination of these characteristics defined the choice of PVA rather than another compound to build a polymeric network to support metallic ions. In addition, PVA is a low-cost, nonionic, biocompatible industrial product with good mechanical properties [26]; ethanol (95%; CH_3CH_2OH); $C_8H_{18}O$ (octanol); deionized water; concentrated HNO_3 solution (65%); concentrated ammonia solution (28–30%; NH_4OH); gases (NH_3, Ar, and H_2); and industrial 304-type stainless steel powder.

2.2. The Nonconventional Powder Metallurgy Process Developed

2.2.1. Manufacture of SS and UO_2 Microspheres. Figure 1 illustrates the nonconventional powder metallurgy process used in the fabrication of both SS and UO_2 microspheres and cermet (SS-UO_2) and SS pellets. It shows the equipment used (description in Supplementary Materials) and summarizes the main steps in the microsphere and pellet manufacture process: hydrogel microsphere production (Figure 1(a)), washing (Figure 1(b)), thermal treatment (Figure 1(c), SS and UO_2 microspheres), mixing metallic and ceramic particles without the need of previously making a suspension with the help of an appropriate agglomerating liquid, e.g., a PVA solution [27]/homogenization for 30 min (Figure 1(d)), pressing (Figure 1(e)), and sintering (Figure 1(f); SS-UO_2 cermet pellet). In Figure 1(a), the *templates* were materials without (*soft*: PVA, urea, ethanol, ammonium nitrate, and

water) or with (*hard*: carbon black nanoparticles) a fixed rigid structure. They were used to generate multiple hollow nuclei in the microspheres [23–25, 28].

The sol–gel process shown in Figure 1(a) shapes hydrogel metal oxyhydroxide microspheres at room temperature. The basic mechanism for shaping the hydrogel microspheres (Figure 1(a)) used as precursors of both SS and UO_2 microspheres is described in Santos et al. [21] and in Oliveira et al. [26]. In short, PVA monomers ($(CH_2CH(OH))_n$) trap Fe, Cr, Ni, U, and carbon black nanoparticles, increase the viscosity of the medium, and enable the shaping of perfect and evenly spaced spherical droplets. In these droplets, chemical reactions in gaseous (NH_3) and liquid (NH_4OH) media promote and/or continue the hydrolysis and the condensation of the Fe, Cr, and Ni (microspheres SSM0 to SSM4$^+$) and U (UOM0 microsphere) cations with each other on the surface of the pre-existing metal oxides and/or the functionalized carbon black nanoparticles. Here, the functionalization of these nanoparticles happened by action of the nitric acid present in the stable colloidal Fe/Cr/Ni dispersion, providing the nanoparticles with carboxylic functional groups (COOH and OH), which improves both their dispersion in aqueous medium and their interaction with metal ions [29]. These referred ammoniacal media are also responsible for the crosslinking and entanglement of the PVA molecules with each other and around the said condensed inorganic and/or naked carbon black nanoparticles. The PVA crosslinking was carried out here with the aid of the physical crosslinking method, but one cannot rule out the effect of the carbon black as a chemical compound producing chemical interaction effects between the PVA molecules (via hydrophobic bonds, for example). The crosslinking of PVA monomers occurred as a result of inducing the formation of its crystallites, which was promoted by ammonia media both by dehydration of water molecules linked to the hydroxyls of PVA molecules by hydrogen bonds and/or by raising the saline concentration of the aqueous medium, in the present case with NH_4NO_3 salt formed *in situ*, where the PVA would have its solubility decreased. Under these conditions, the formation of hydrogen bonds between PVA molecules, PVA molecules/inorganic nanoparticles, and/or PVA molecules/carbon black nanoparticles is favored. These interactions and the introduction of materials with higher mechanical strength are decisive in increasing the mechanical strength of the resulting polymeric membrane [26, 30–34]. This results in monodisperse hydrogel microspheres with defined diameters and sufficient mechanical rigidity to maintain integrity and sphericity in the subsequent processing steps. It is important to point out that this process favored the mixing of Fe, Cr, and Ni SS precursor element particles at a molecular level and facilitated their interaction with molecules (H_2O, PVA) and other compounds (carbon black, NH_4NO_3). In this interaction, intermolecular forces (dispersion or London-van der Waals forces (0.05–20$^+$ kJ/mol), dipole–dipole forces (3–20$^+$ kJ/mol), hydrogen bonding forces (10–40 kJ/mol), and ion-dipole forces (30–100$^+$ kJ/mol)), responsible for maintaining the condensed state of matter (liquid and solid), enabled the creation of interfaces between the constituents of the hydrogel microspheres [27, 35–37].

Six batches of SS (SSM0, SSM1, SSM3, SSM4, and SSM4$^+$) and UO_2 (UOM0) microspheres were manufactured. Stable colloidal dispersions of Fe/Cr/Ni and U were obtained by heating them up to 363 K and cooling them down to 323 K. The Fe/Cr/Ni colloidal dispersion (300 mL) was composed of Fe stock solution (128.0 g) + $Cr(NO_3)_3{\cdot}9H_2O$ (28.0 g) + $Ni(NO_3)_2{\cdot}6H_2O$ (24.5 g) + urea (112.0 g) + deionized water (100.0 g). To this colloidal dispersion, carbon black nanoparticles (diameters $\leq$45 nm; 0.0 g (SSM0) or 1.5 g (SSM1) or 3.0 g (SSM3) or 4.5 g (SSM4, SSM4$^+$)) + ethanol (3.9 g) + PVA solution (90.0 g) + octanol (two drops) were added. The Fe stock solution (158.2 ± 5.2 gFe/L and 100.5 ± 3.3 gFe/kg) was obtained from a mixture of $Fe(NO_3)_3{\cdot}9H_2O$ (2,000.0 g) + concentrated HNO_3 solution (400 mL) + deionized water (2,400.0 g) at 363 K after distillation of 2,000.0 g of water. The PVA solution (79.0 ± 1.2 gPVA/kg and 77.1 ± 1.0 gPVA/L) was obtained from a mixture of PVA (320.0 g) + deionized water (3,760.0 g) at 363 K. The U colloidal dispersion (200 mL) was composed of $UO_2(NO_3)_2{\cdot}6H_2O$ stock solution (153.2 g) + NH_4NO_3 (41.2 g) + urea (50.4 g) + deionized water (50.0 g). To this U colloidal dispersion, carbon black nanoparticles (0.0 g (UOM0)) + ethanol (14.1 g) + PVA solution (47.8 g) + octanol (two drops) were added. The $UO_2(NO_3)_2{\cdot}6H_2O$ stock solution (326.5 ± 5.2 gU/kg and 563.9 ± 9.0 gU/L) was obtained from a mixture of $UO_2(NO_3)_2{\cdot}6H_2O$ (4,483.2 g) + deionized water (2,000.0 g) at 303 K. These two types of dispersions, Fe/Cr/Ni and U dispersions, were individually dripped into gaseous (NH_3; ammonia flow rate at a maximum value of 9 NL/min at 298 K and 100 kPa) and ammoniacal (NH_4OH) media, using 287 and 368 μm nozzles, respectively. The hydrogel microspheres were aged in ammoniacal medium at 303 K/12 hr (SSM0h, SSM1h, SSM3h, SSM4h, SSM4$^+$h, and UOM0h) and at 338 K/2 hr (SSM0h to SSM4$^+$h) (Figure 1(a)). They were washed (Figure 1(b)) with deionized water to eliminate NH_4NO_3, kept immersed in deionized water, characterized, and used for controlled thermal treatment (Figure 1(c)) and fabrication of the cermet-type pellets. The procedure for adjusting the Ni content in the SSM4h microsphere, resulting in the SSM4$^+$h microsphere, is given in the Supplementary Materials. Table S1 shows the carbon black content (CBC) and drying parameters of the hydrogel microspheres. It details the drying conditions of the hydrogel microspheres. Briefly, SSM0h–UOM0h were dried at 303 K (SSM0x-SSM4$^+$x) and at 303 + 373 K (UOM0x). Table S2 shows the sintering (si) and/or calcination (c) and/or reduction (r) sequential thermal treatment (STT) parameters (T(K)/atm./DT(hr)/HR(K/min)/CM) of the xerogel microspheres. It details the thermal treatment conditions of the xerogel microspheres. Briefly, SSM0x was reduced at 1,273 K/H_2/2 hr (SSM0r1) and at 1,523 K/H_2/2 hr (SSM0r2). SSM1x-SSM4$^+$x were sintered (1,273 K/Ar/2 hr, SSM1si-SSM4$^+$si), calcined (1,173 K/air/3 hr, SSM1c3, SSM3c3, SSM4c3, and SSM4$^+$c3; 873 K/air/3 hr (SSM4c1); and 873 K/Air/24 hr (SSM4c2)), and reduced (1,073 K/H_2/2 hr, SSM1c3r, SSM3c3r, SSM4c1r, SSM4c2r, SSM4c3r, and SSM4$^+$c3r). These three calcination conditions used sought both to determine the appropriate temperature/time condition to maximize carbon black elimination and to verify its effect on

metallic particle growth within the resulting porous microsphere. UOM0x was sintered (1,913 K/H_2/2 hr, UOM0si). Ultrapure (99.999%) H_2 or Ar flow rate was used at a maximum value of 0.4 NL/min at 298 K and 343 kPa. The cooling speed of the SS and UO_2 microspheres was regulated by the thermal inertia of the tube furnace refractories (Figure 1(e)) and by the room temperature (291–303 K).

2.2.2. Manufacture of the SS-UO_2 Cermet (PCERM1–PCERM5) and SS (PSS1) Pellets. Manufacturing cermet pellets requires mixing and homogenizing (Figure 1(d)) volumetric fractions of SS and UO_2 microspheres, compacting (Figure 1(e)) the microspheres into the desired cylindrical shape, and sintering (Figure 1(f)) the resulting green pellet. In sintering, the green pellet is heated to a temperature below the metallic alloy melting point, a temperature at which solid state bonds occur between the ceramic and metallic microspheres, eliminating the pores formed and densifying the resulting cermet pellet [6, 16]. Table S3 shows the SS-UO_2 and SS pellet pressing parameters. It details the 58 vol% SS-42 vol% UO_2 and 100 vol% SS pellet pressing parameters, highlighting the composition of PCERM1 (UOM0si + SSM0r1), PCERM2 (UOM0si + SSM4c1r), PCERM3 (UOM0si + SSM4c2r), PCERM4 (UOM0si + SSM4c3r), PCERM5 (UOM0si + SSM4c3r), and PSS1 ($SSM4^+c3r$). The choice of PCERM1–PCERM5 compositions aimed to show the effect of porosity and metallic particle size growth inside the SS microspheres on the quality of the interface created between the dissimilar materials SS and UO_2 [27]; in the case of the steel pellet PSS1, we sought to confirm the total reducibility of metallic oxides in the SS precursor microspheres with increasing temperature. Table S4 shows the sequential thermal treatment (STT) parameters of the SS-UO_2 cermet and SS pellets. It details the STT parameters of these pellets. Briefly, the pellets were sintered at 1,273 K/H_2/0.08 hr and 1,623 K/H_2/2.0 hr (PCERM1), 1,523 K/H_2/0.08 hr and 1,703 K/H_2/2.0 hr (PCERM2, PCERM3, and PCERM4), and 1,523 K/H_2/2.0 hr and 1,703 K/H_2/4.0 hr (PCERM5 and PSS1). A maximum flow rate of ultrapure (99.999%) H_2 of 0.4 NL/min was used at 298 K and 343 kPa. The cooling rate of the PCERM1–PCERM5 and PSS1 pellets was regulated by the thermal inertia of the tube furnace refractories (Figure 1(f)) and the room temperature (291–303 K).

2.3. Characterizations. Diameter range (D (μm)) and sphericity ($= D_{\text{smallest}}/D_{\text{largest}}$ ($\equiv D_S/D_L$)) were measured by optical comparator images of 17 microspheres. The macrostructural and microstructural aspect examinations were carried out by an optical microscope (OM analysis, optical microscopy, Zeiss brand/STEMI 200-C model) and a scanning electron microscope (SEM analysis, scanning electron microscopy, Carl Zeiss Microscope, SIGMA VP model), respectively. The qualitative evaluation of the compressive behavior of the SS and UO_2 microspheres was limited to obtaining the mechanical resistance to compression (MR; i.e., the compressive stress) of 20 microspheres using a 882-type Universal Instron machine and applying a compression force of 10 N; ASTM standards were not found to support a complete evaluation of the mechanical properties of spherical bodies with a diameter in the micron size range. The volumetric shrinkage of the hydrogel to xerogel (VS_X) and to thermally treated (VS_{TT}) microspheres was mathematically calculated using the volume change of 20 microspheres. The geometric density of the microspheres (ρ_{spheres} (g/cm^3/%TD)) was calculated using the mass/volume ratio of 200 microspheres and considering the theoretical density (TD) values for UO_2 (ρUO_2, 10.97 g/cm^3 [5]) and SS (ρSS, 7.90 g/cm^3 [6, 10]). The porosity (P(%)) associated with the densification level reached in the SS and UO_2 microspheres was deducted from the calculated theoretical density values [6]. The CBC (independent variable X) effect on the macrostructural characteristics of SS microspheres (dependent variable Y) was discussed and qualitatively evaluated. For this evaluation, the statistical terminology taught and simplified by Costa [38] was used. When the variables X and Y of the line equation $Y = b + aX$ vary in the same direction, a positive line slope is obtained; when the variations are in opposite directions, a negative line slope is obtained. The correlation between X and Y was graded using the linear correlation coefficient (R^2) as follows: $R^2 \cong +1.00$, perfect positive correlation; $0.75 < R^2 < 1.00$, strong positive correlation; $0.50 < R^2 < 0.75$, mean positive correlation; $0.25 < R^2 < 0.50$, weak positive correlation; $0.00 < R^2 < 0.25$, nonexistent linear correlation. The line equation and R^2 have been included in the graphs provided. The geometric density of the cermet pellets (ρ_{pellet} (g/cm^3/%TD)) was calculated using the mass/volume of each pellet and considering both the referred theoretical density (TD) values for UO_2 and SS (ρUO_2 and ρSS) and the equation ρ_{pellet} (g/cm^3) $= \rho UO_2 \times 0.42 + \rho SS \times 0.58$ [4] in the calculation performed. The analysis of the mechanical properties of the cermet pellets was limited to a qualitative observation of their wear resistance [27] during the ceramographic preparation to perform the SEM analysis. The elemental compositions of the xerogel and the thermally treated xerogel microspheres and the pellets were obtained using energy dispersive X-ray fluorescence spectroscopy (EDX analysis; Shimadzu, model EDX-720, Si detector) and/or energy dispersive spectroscopy (EDS analysis; Bruker Nano GmbH, model XFlash Detector 410-M). The X-ray diffraction pattern of SS and UO_2 microspheres was obtained using CuKα radiation ($\lambda = 1.54178$ Å) in a Rigaku diffractometer/mod. Geigerflex over a 2θ range between 20° and 80°.

3. Results and Discussion

3.1. Main Physical and Chemical Characteristics of the SS and UO_2 Microspheres. The central idea of this R&D was to produce a SS microsphere that fragments without damaging the UO_2 microsphere during the pellet pressing process. This *in situ* micronization effect was obtained with the use of carbon black nanoparticles in the formulation of the metallic particle precursors and their appropriate thermal treatment. *In situ* micronization refers to a particle engineering technique where micrometer-sized or smaller crystals are obtained during their production itself, without the need for additional size reduction or the use of special equipment [39].

The production of chemically stable Fe/Cr/Ni and U colloidal dispersions inhibited the partial clogging of the dosing nozzle (Figure 1(a)) and ensured the formation of

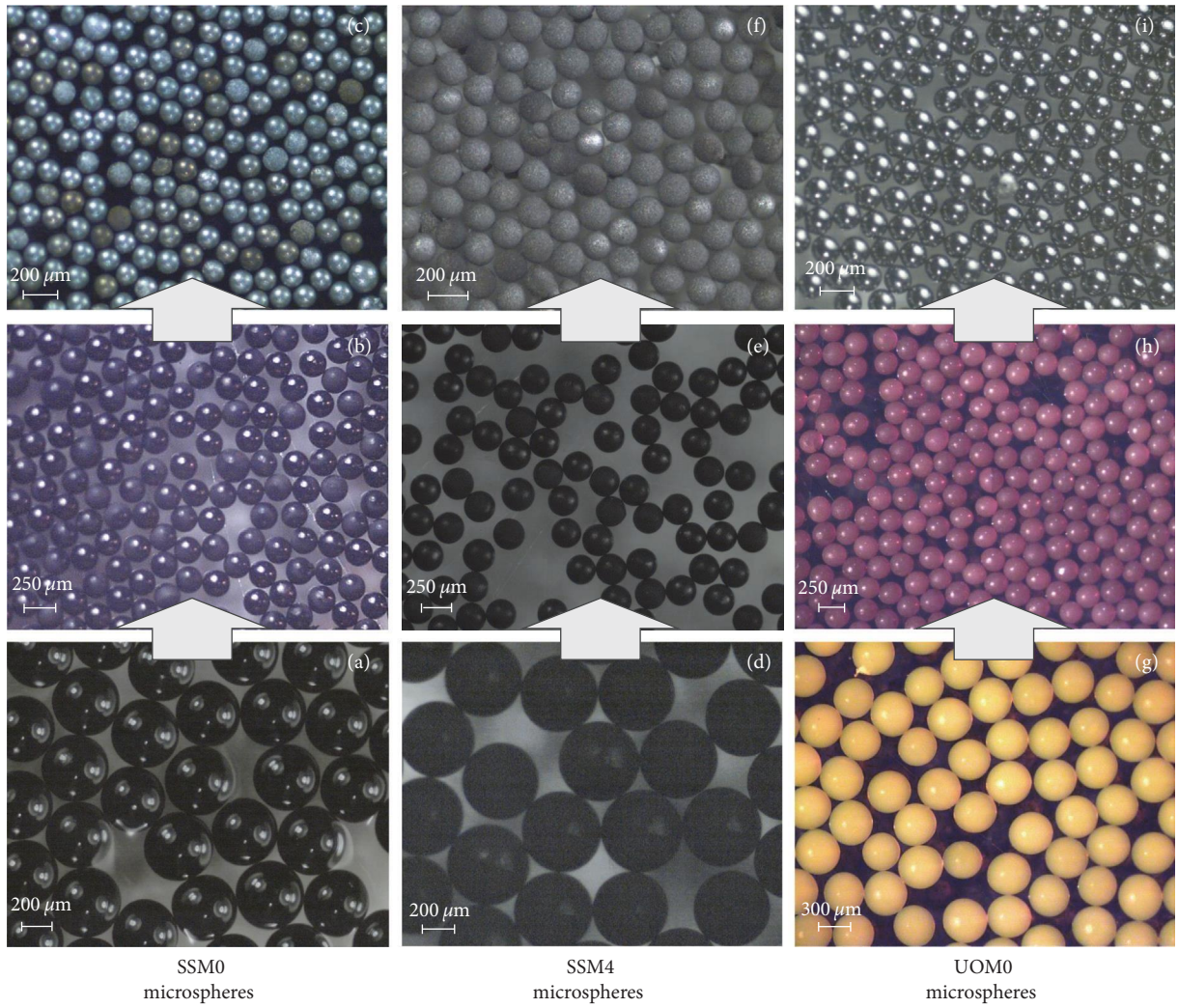

FIGURE 2: Illustrations of the macrostructural characteristics of the dissimilar SS and UO_2 particles produced with or without the addition of carbon black: (a) SSM0h; (b) SSM0x; (c) SSM0r1; (d) SSM4h; (e) SSM4x; (f) SSM4c1r; (g) UOM0h; (h) UOM0x; (i) UOM0si. OM images.

the hydrogel (Figures 2(a)(SSM0h), 2(d)(SSM4h), 2(g)(UOM0h)), of the dried (Figures 2(b)(SSM0x), 2(e)(SSM4x), 2(h)(UOM0x)), and of the thermally treated xerogel (Figures 2(c)(SSM0r1), 2(f)(SSM4c1r), 2(i)(UOM0si)) microspheres with high sphericity and low diameter size dispersion, that is, monodisperse microspheres. The resulting color of the hydrogel microspheres without (black, Figure 2(a)) or with (black, Figure 2(d)) carbon black evidenced the mixing of the Fe (dark brown), Cr (green), and Ni (greenish black), and U (orange, Figure 2(g)) oxyhydroxides in the PVA polymeric network at molecular level. Dehydration of the microspheres induced the formation of pores, which either accentuated (Figures 2(b) and 2(e)) or masked (Figure 2(h)) the original color of the compound. The elimination of the carbon black increased the formation of pores, explaining the masking of the shiny grayish-silver color of the SS (Figures 2(c) and 2(f)); the elimination of pores highlighted the black color of UO_2.

Figure 3 shows the CBC effect on the characteristics of the SS microspheres. For the hydrogel microspheres (Table 1), the effect on diameter (Figure 3(a)) was positive, but without correlation ($R^2 = 0.2186$), which suggested the future need to consider a multifactorial influence on it and the other characteristics analyzed. Sphericity (Figure 3(b)) and compressive stress (Figure 3(c)) suffered a negative effect with a strong ($R^2 = 0.8000$ and $R^2 = 0.8095$, respectively) correlation. These characteristics depended almost exclusively on the good elastic behavior (the stress/strain ratio has not been determined) of the PVA crosslinked network, which was affected by both the change in local porosity and the action of hydrophobic forces on the carbon black/PVA interface created. Hydrophobic forces are weaker than the hydrogen bonds acting at the PVA/H_2O, PVA/PVA, and PVA/metallic oxyhydroxides interfaces. Note that the compressive stress decreased from 14.9 ± 2.1 to 11.2 ± 1.8 MPa, reflecting a reduction in microsphere rigidity [27, 30, 31, 33, 35, 37, 38, 40].

For the xerogel microspheres (Table 2), the positive effect on diameter (Figure 3(d)) did not correlate ($R^2 = 0.1988$) with the CBC. However, the homogeneous distribution of carbon black helped the metallic oxyhydroxides to avoid the

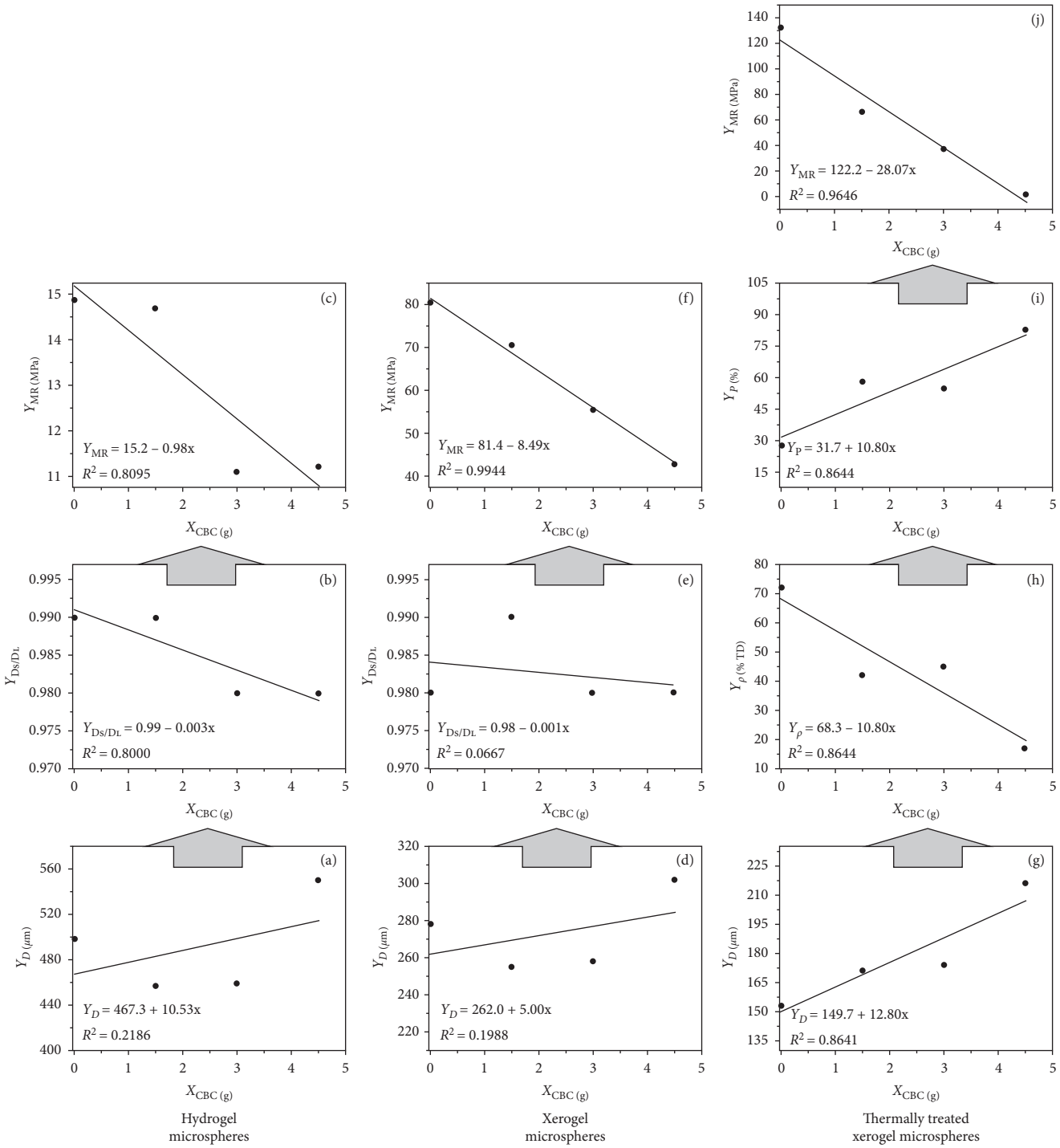

FIGURE 3: Quantification of the carbon black content effect on the macrostructural characteristics of the SS microspheres: (a)–(c) hydrogel, (d)–(f) xerogel, and (g)–(j) thermally treated xerogel (SSM0r1, SSM1c3r, SSM3c3r, and SSM4c3r) microspheres.

deleterious effects of cracking and/or fragmentation on the microspheres (Figures 2(b) and 2(e)) due to their volumetric contraction (∼83%). The effect on sphericity (Figure 3(e)) and compressive stress (Figure 3(f)) was negative, but with no ($R^2 = 0.0667$) and perfect ($R^2 = 0.9944$) correlation with the CBC, respectively. Dehydration increased PVA crosslinking, that is, it increased the domain of hydrogen bonds at the PVA/PVA and PVA/metallic oxyhydroxides interfaces, that is, it crystallized and hardened the polymeric network. In addition, it also increased the local porosity and the action of hydrophobic forces at the carbon black/PVA interface. Note that the compressive stress decreased from 80.3 ± 6.6 to 42.8 ± 5.4 MPa [27, 30, 31, 35, 37, 38, 40].

To the analysis of the macrostructural characteristics of the thermally treated xerogel microspheres (Table 3), an evaluation of the microstructural characteristics of the microspheres

Table 1: Effect of the carbon black content on the macrostructural characteristics analyzed of the SS and UO_2 precursor hydrogel microspheres.

Codes	CBC (g)	Physical characteristics*		
		D (μm)	D_S/D_L	MR (MPa)
SSM0h	0.0	498 ± 9	0.99	14.9 ± 2.1
SSM1h	1.5	457 ± 12	0.99	14.7 ± 2.3
SSM3h	3.0	459 ± 11	0.98	11.1 ± 2.4
SSM4h	4.5	550 ± 4	0.98	11.2 ± 1.8
$SSM4^+h$	4.5	550 ± 4	0.98	11.2 ± 1.8
UOM0h	0.0	455 ± 13	0.98	>55.5

*CBC, carbon black content; D (μm), diameter; D_S/D_L, sphericity; MR (MPa), mechanical resistance to compression.

Table 2: Effect of the carbon black content on the macrostructural characteristics of the SS and UO_2 precursor xerogel microspheres analyzed.

Codes	CBC (g)	Physical characteristics*			
		D (μm)	D_S/D_L	VS_X	MR (MPa)
SSM0x	0.0	278 ± 7	0.98	83	80.3 ± 6.6
SSM1x	1.5	255 ± 6	0.99	83	70.4 ± 2.4
SSM3x	3.0	258 ± 5	0.98	82	55.5 ± 9.7
SSM4x	4.5	302 ± 7	0.98	83	42.8 ± 5.4
$SSM4^+x$	4.5	302 ± 7	0.98	83	42.8 ± 5.4
UOM0x	0.0	274 ± 9	0.95	78	38.3 ± 4.1

*CBC, carbon black content; D (μm), diameter; D_S/D_L, sphericity; VS_X, volumetric shrinkage of the xerogel microspheres; MR (MPa), mechanical resistance to compression.

Table 3: Effect of the carbon black content on the macrostructural characteristics of the thermally treated xerogel microsphere precursors of SS and UO_2 analyzed.

Codes	CBC (g)	Physical characteristics*		
		D (μm)/D_S/D_L/VS_{TT}	$\rho_{spheres}$ (g/cm^3)/(%TD)/P (%)	$D_{gigapores}$ (μm)/$D_{particles}$ (μm)/MR (MPa)
SSM0r1	0.0	153 ± 5/0.99/83	5.8/72/28	0.9 ± 0.3/-/132.2 ± 24.7
SSM0r2	0.0	-/-/-	-/-/-	-/-/-
SSM1c3r	1.5	171 ± 5/0.98/70	3.3/42/58	-/-/66.3 ± 11.2
SSM3c3r	3.0	174 ± 4/0.99/69	3.5/45/55	-/-/37.0 ± 5.0
SSM4c1r	4.5	190 ± 13/0.97/75	2.3/29/71	1.7 ± 0.9/1.6 ± 0.6/11.0 ± 3.3
SSM4c2r	4.5	210 ± 6/0.98/66	1.8/23/77	-/-/0.5 ± 0.2
SSM4c3r	4.5	216 ± 10/0.98/63	1.3/17/83	1.5 ± 0.6/3.1 ± 1.4/1.3 ± 0.4
$SSM4^+c3r$	4.5	-/-/-	-/-/-	-/-/-
UOM0si	0.0	176 ± 6/0.96/73	10.9/99/1	-/3.5 ± 1.5/147.4 ± 25.0

*CBC, carbon black content; D (μm), diameter; D_S/D_L, sphericity; MR (MPa), mechanical resistance to compression; $\rho_{spheres}$ (g/cm^3)/(%TD)/P(%), apparent density of the microspheres; %TD, theoretical density; P(%), porosity; $D_{gigapores}$ (μm), gigapore diameter; $D_{particles}$, particle diameter; VS_{TT}, volumetric shrinkage of the thermally treated xerogel microspheres.

SSM0r1 (Figures 4(a)–4(a2)), SSM4c1r (Figures 4(b)–4(b2)), SSM4c3r (Figures 4(c)–4(c2)), and UOM0si (Figures 4(d)–4(d2)) was added. The positive effect on diameter (Figure 3(g)) was accompanied by a strong correlation ($R^2 = 0.8641$). The pores formed modulated the volumetric shrinkage (see V_{STT} in Table 3) without generating visible cracks (Figures 4(a–a2) to 4(d–d2)). The resulting porosity in the SS microspheres contained irregular-shaped gigapores (see circles in Figures 4(a2)–4(c2)) with an estimated diameter of $0.9 \pm 0.3\,\mu$m (SSM0r1, Figure 4(a2)), $1.7 \pm 0.9\,\mu$m (SSM4c1r, Figure 4(b2)), and $1.5 \pm 0.6\,\mu$m (SSM4c3r, Figure 4(c2)); uranium microspheres (Figure 4(d2)) do not exhibit visible pores. Gigapores refer to pores >100 nm in size [26]. The negative effect ($y = 0.98 - 0.001x$) on sphericity showed no correlation ($R^2 = 0.2000$) with the CBC. Note that the elimination of templates and the sintering and oxide–metal conversion processes that took place stiffened the resulting inorganic network. This stiffening was linked to the sintering mechanisms of formation and thickening of necks between particles and the closing, rounding, and elimination of pores in the final densification. Stiffening was also connected with the formation of oxide/oxide, metal/oxide, and metal/metal interfaces, where covalent or ionic/covalent or ionic, metallic/covalent or ionic, and metallic/metallic chemical bonds, respectively, much stronger than hydrogen bonds, came to predominate [27, 35, 37, 40]. The negative effect on *density* (Figure 3(h)) had a strong

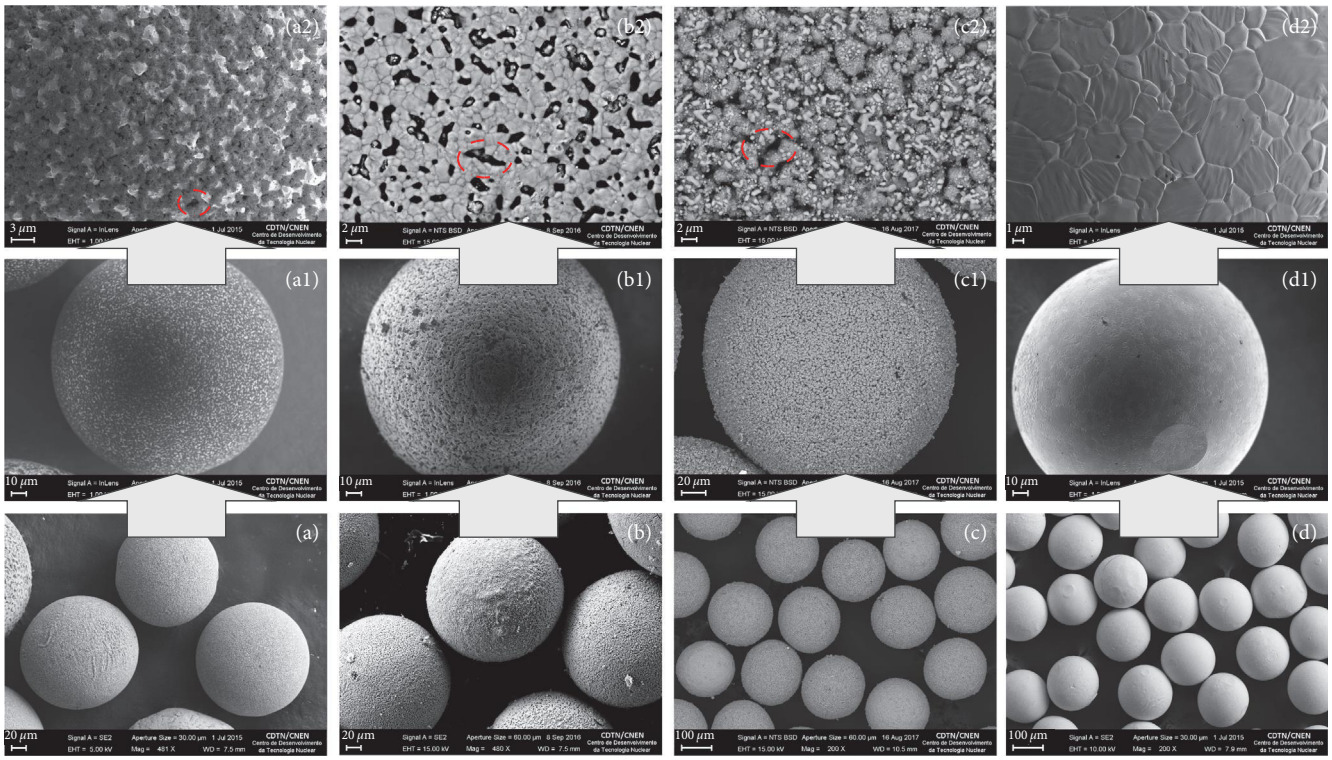

FIGURE 4: Illustrations of the microstructural characteristics of the dissimilar SS and UO_2 particles produced with or without the addition of carbon black: (a, a1, a2) SSM0r1; (b, b1, b2) SSM4c1r; (c, c1, c2) SSM4c3r; and (d, d1, d2) UOM0si. SEM images. Scale bar values: (a, 20 μm), (a1, 10 μm), (a2, 3 μm); (b, 20 μm), (b1, 10 μm), (b2, 2 μm); (c, 100 μm), (c1, 20 μm), (c2, 2 μm); and (d, 100 μm), (d1, 10 μm), (d2, 1 μm).

($R^2 = 0.8644$) correlation with the CBC. This is consistent with the gradual loss of mass of the templates in the microsphere and the preservation of its volume. It is important to point out that the density of the UO_2 microsphere can be reduced from 99% TD (1% porosity) to the usual 94%–96% TD (6%–4% pores) with the introduction of carbon black in its production. This remaining porosity minimizes the release of the fission gas, accommodates fuel swelling, and prevents in-pile densification [4, 20]. The positive effect on porosity (Figure 3(i)) was strongly correlated ($R^2 = 0.8644$) with the CBC. In this case, this imperfect correlation may be revealing the occurrence of pore closure both by liquid phase sintering and by mass transfer by diffusion and/or viscous flow. The liquid phase could be produced in the local melting process of the metallic nanoparticles at the metal/oxide interface [40, 41]. The negative effect on compressive stress (Figure 3(j)) was strongly correlated ($R^2 = 0.9646$) with the CBC. This almost perfect correlation explains the dependence of the compressive stress on the thickening of the necks between particles inside the microsphere. This thickening decreased with an increase in the amount and homogeneous distribution of pores within the microsphere. This made the necks points of weakness in the microsphere, favoring *in situ* micronization. Note that the *in situ* micronization and sintering processes generated shapeless micrometer particles (size not determined for SSM0r1, Figure 4(a2); $1.6 \pm 0.6\,\mu$m, SSM4c1r, Figure 4(b2); and $3.1 \pm 1.4\,\mu$m, SSM4c3r, Figure 4(c2)) separated by pores and connected to each other by necks inside the large microspheres ($153 \pm 5\,\mu$m, SSM0r1, Figures 4(a) and 4(a1); $190 \pm 13\,\mu$m, SSM4c1r, Figures 4(b) and 4(b1); and $216 \pm 10\,\mu$m, SSM4c3r, Figures 4(c) and 4(c1)). Also, note that there was an increase in particle size within the microsphere (from $1.6 \pm 0.6\,\mu$m (Figure 4(b2)) to $3.1 \pm 1.4\,\mu$m (Figure 4(c2)) with increasing calcination temperature (from 873 to 1,173 K/3 hr). In the UOM0si microsphere (Figures 4(d)–4(d2)), the growth of the precursor nanoparticles at 1,913 K/2 hr was limited ($3.5 \pm 1.5\,\mu$m; Figure 4(d2)) and equiaxed grains formed [42]. *In situ* micronization endowed the SSM4c1r (Figures 4(b) and 4(b1), 11.0 ± 3.3 MPa) and SSM4c3r (Figures 4(c) and 4(c1), 1.3 ± 0.4 MPa) soft SS microspheres with a brittle behavior, high compressibility, and a small particle size proper to facilitate the processes of plastic deformation or liquid phase or diffusion or viscous flow during pressing and sintering of the SS-UO_2 pellets. These processes promoted the adherence of the SS to the surface of the rigid inclusions represented by the SSM0r1 (132.2 ± 24.7 MPa) and UOM0si (147.4 ± 25.0 MPa) hard microspheres. This facilitated the generation of a metal/ceramic interface with good interaction quality, i.e., without discontinuities such as cracks and pores along the interface [4, 27, 40–43]. Soft microspheres mean compressible and sinterable microspheres [43]. *Rigid inclusion* refers to the incompressible and non-sinterable behavior of a hard particle in the matrix of a composite that causes a large drop in its densification rate [43]. Figure 5

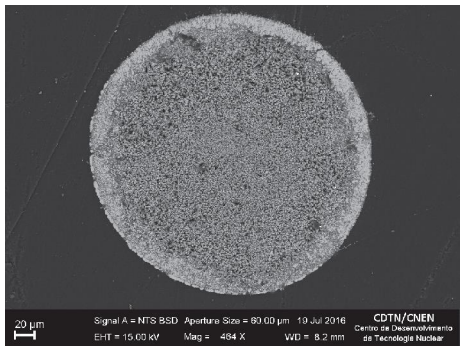

FIGURE 5: Easy *in situ* micronization of the microparticle agglomerate in the porous core of the SSM4c1r microsphere with plain light sanding.

presents the materialization of the *in situ* micronization idea. This figure shows the soft embedded and polished SSM4c1r microsphere (Figures 4(b)–4(b2)). It exhibits an agglomerate of microparticles ($1.6 \pm 0.6\,\mu$m) with a shiny grayish-silver color of SS in the porous ($1.7 \pm 0.9\,\mu$m) core, surrounded by a denser layer ($\sim 20\,\mu$m), which easily micronized with plain light sanding.

Figure 6 shows the dependence of oxide-metal conversion on increasing reduction temperature in the SSM0 microsphere (Table S2; more information in the Supplementary Material). At 303 K (Figure 6(a), SSM0x), characteristic amorphous metallic oxyhydroxides were obtained with predominant ferrihydrite phase, $Fe_5HO_8{\cdot}4H_2O$ [26]. At 1,273 K (Figure 6(b), SSM0r1), significant but partial oxide–metal conversion was seen. The Fe–Cr–Ni alloy was formed alongside the remaining Fe_2O_3 and Cr_2O_3 phases. The alloy peaks at 44.48° (110) and 64.48° (200) correspond to the martensite phase (α-Fe + cementite (Fe_3C; hard and brittle phase)), at 50.84° (200), this peak corresponds to the austenite phase (γ-Fe). Martensite has been considered a supersaturated solid carbon solution in the α-Fe phase (ductile phase), the carbon content of which can vary from 0.008% to 2.11% C. These phases occur at specific temperatures (α-Fe, $\leq$1,185 K; γ-Fe, 1,185 K–1,667 K; δ-Fe, 1,667 K–1,811 K; and liquid Fe^0, $\geq$1,811 K) and under specific cooling conditions [44, 45]. Thus, the intensity of the peak at 44.48° (110) suggests that the cooling speed of the microspheres (from 1,273 to <1,185 K) was fast enough to promote an almost complete transformation of austenite into martensite. At 1,523 K (Figure 6(c), SSM0r2), the oxide–metal conversion increased, but now only the Cr_2O_3 oxide phase remained. Note that the cooling rate was sufficiently slow (from 1,523 to <1,185 K) to inhibit the transformation of austenite (43.50° (110), 50.84° (200), and 74.50° (220)) into martensite (44.48° (110) and 64.48° (200)) [17, 44, 45]. Also note that the diffraction pattern of the SSM0r2 microsphere (Figure 6(c)) is very similar to that of the industrial SS powder (Figure 6(d); cooling from 1,813 to <1,185 K), but still peaks at 64.48 (200), suggesting that the total oxide–metal conversion will require a better adjustment of the temperature/time of the processes of reduction, interdiffusion of the alloy microconstituents, and cooling that happen during the thermal treating of the SS microspheres [16, 17, 44, 45]. It is important to emphasize that the cooling conditions influence the final texture of the SS significantly. Continuous cooling induces the formation of the microconstituents martensite (characterized by a thin and narrow plate structure) and pearlite (also a mixture of α-Fe and cementite phases, characterized by a lamellar structure). Isothermal cooling forms bainite (also a mixture of α-Fe and cementite phases, characterized by a thin and narrow plate structure). Another influence comes from the constituents of the SS. C and Cr stabilize the α-Fe phase, while Ni reinforces the transformation of the α-Fe phase into the γ-Fe phase [16, 44, 45]. Therefore, even though total conversion has not been achieved, this result anticipated the fact that obtaining dense or porous 304-type stainless steel microspheres is a feasible task.

Figure 7 confirms the dependence of the oxide–metal conversion on the heat treatment conditions now applied to the SSM4 and UOM0 microspheres. At 303 K (Figure 7(a), SSM4x), the amorphous phase, ferrihydrite ($Fe_5HO_8{\cdot}4H_2O$), predominated [26]. At 373 K (Figure 7(f), UOM0x), the metaschoepite phase, $UO_3{\cdot}1{\cdot}5H_2O$, was identified [46]; UOM0x was formed by nanoparticles with a diameter in the order of 7.5 nm (as determined by the Scherrer equation). In the SSM4 microsphere, previously sintered at 1,273 K/Ar/2 hr (SSM4si), the formation of the martensite phase (44.48° (110) and 64.48° (200)) was observed alongside the oxide phases Cr_2O_3, Fe_2O_3, and $NiFe_2O_4$, even though it was calcined at 873 K/Air/3 hr (Figure 7(b), SSM4c1). CO formed *in situ* played an important role in the reported reduction. Subsequently, with the reduction at 1,073 K (Figure 7(c), SSM4c1r), the oxide-metal conversion increased, now forming martensite (44.48° (110) and 64.48° (200); predominant) and austenite (43.50° (110) and 50.84° (200); incipient), with the Cr_2O_3 and Fe_2O_3 phases remaining. The calcinations performed at 873 K/Air/24 hr (Figure not shown, SSM4c2) and at 1,173 K/Air/3 hr (Figure 7(d), SSM4c3) completely reoxidized the martensite formed in the previous sintering under Ar, forming phases Cr_2O_3, Fe_2O_3, and $NiFe_2O_4$. The result of the reduction in the SSM4c2 (Figure not shown, SSM4c2r) and the SSM4c3 (Figure 7(e), SSM4c3r) microspheres was virtually the same as that of the martensitic SSM4c1r microspheres (Figure 7(c)). In the UOM0x microspheres, direct sintering at 1,913 K/H_2/2 hr (Figure 7(g)) promoted high densification (Figures 4(d)–4(d2)), possibly with the help of liquid phase sintering of U^0 [16, 40, 47, 48]. This possibility is real. The high temperature (1,913 K) and ultrapure hydrogen used (wet hydrogen is used in conventional sintering) may have favored an undesirable formation of hypostoichiometric UO_2, which may have decomposed during cooling (from 1,913 to 1,573 K) and formed U^0 [8, 47, 48]. In this case, the heat treatment may have produced a U^0-UO_2-type cermet microsphere with a positive impact on the quality of the SS/U^0-UO_2 interface.

The evolution of the chemical composition of the SS and UO_2 microspheres was determined by either EDX or EDS analyses (Table 4) and illustrated with the EDS spectra in Figure 8. The EDX analysis showed that the compositions of SSM0x, SSM1c3, SSM3c3, SSM4c1, and SSM4c3 were outside the typical range of the industrial 304-type stainless steel powder relative to the elements Fe, Cr, and Ni ((74–70)%

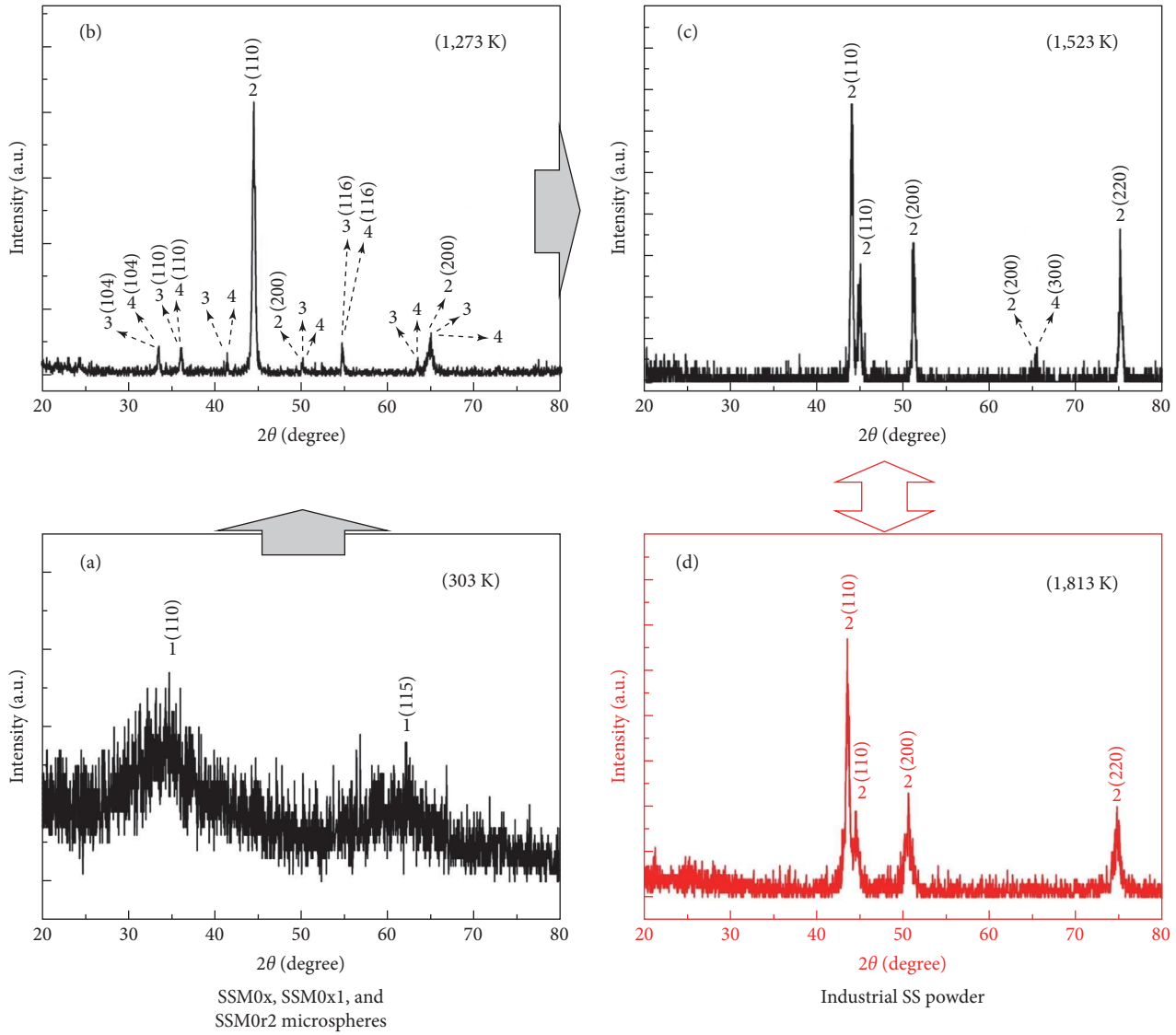

Figure 6: XRD patterns showing the evolution of oxide–metal conversion in SSM0 microspheres with increasing reduction temperature: (a) SSM0x; (b) SSM0r1; (c) SSM0r2; (d) industrial 304-type stainless steel powder. 1 = Ferrihydrite, $Fe_5HO_8{\cdot}4H_2O$; 2 = Fe–Cr–Ni alloy; 3 = Fe_2O_3; 4 = Cr_2O_3.

Fe-(18–20)% Cr-(8–10)% Ni), such as that of the composition of SSM0x (71% Fe-21% Cr-6% Ni-2% Si). This evidenced the loss of nickel in the manufacturing process. The presence of Si can be attributed to spurious contamination [49]. According to Reed [49], the values provided by the EDS analysis must be relativized, since they may be masked by the superimposition of a neighboring element line (Fe, Kα, for example) to the line of another element (Cr, Kβ, for example); seen in Figure 8(a)–8(d). A typical example of this situation of overlapping peaks can be seen in the spectrum in Figure 8(b) (SSM4c1r), which shows lower values of Cr (7%) and Ni (2%), and the nondetection of oxygen, although, in the case of the oxygen, the XRD analysis confirmed the residual presence of Fe_2O_3 and Cr_2O_3 (Figure 7(c)). With this in mind, an EDS analysis performed on the reduced SS microspheres confirmed the loss of Ni; see, for example, the composition of the SSM0r1 microsphere (64% Fe-21% Cr-5% Ni-<1% Si). However, this loss of Ni could be remedied (see Supplementary Material), as demonstrated by the $SSM4^+c3r$ microsphere, 72% Fe-18% Cr-10% Ni (Figure 8(d)).

In SSM0r1 (Figure 8(a)), SSM4c1r (Figure 8(b)), and SSM4c3r (Figure 8(c)), the analyzed oxygen content was 8%, undetected, and 12%, respectively. In addition to the mentioned peak overlapping issue, these values may be suggestive of a greater difficulty for H_2 and/or CO to solubilize and diffuse in the closed pore structure of the microsphere metal–ceramic composite and to react with the remaining metallic oxide inside [40]. Apparently, this difficulty was overcome by raising the temperature in both the reduction of the $SSM4^+c3r$ microsphere (PSS1 pellet component, Figure 8(d);

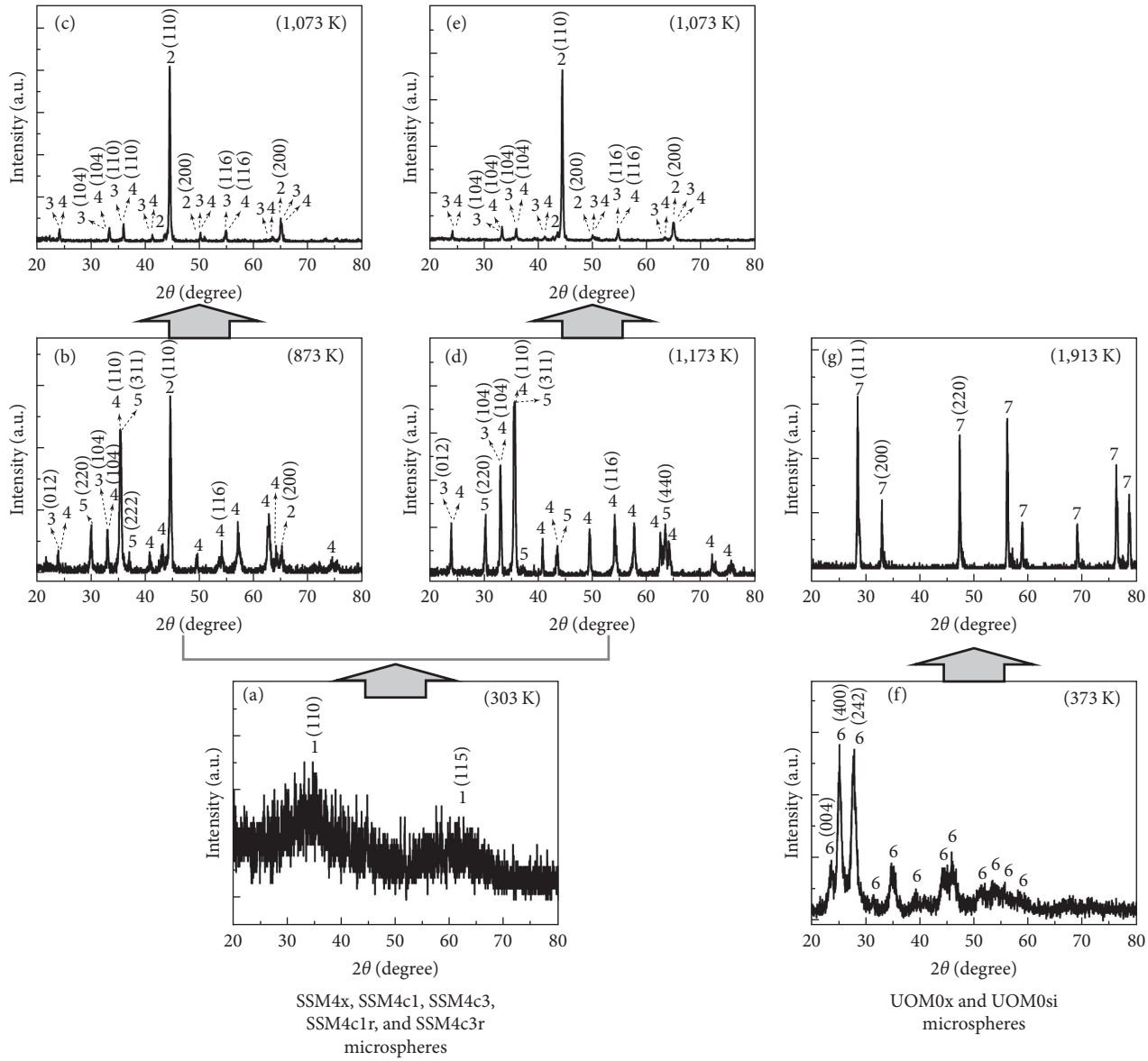

FIGURE 7: XRD patterns showing the effect of the calcination conditions on the evolution of the oxide–metal conversion into the microspheres containing SSM4 carbon black-enriched microsphere and into the UOM0 microsphere: (a) SSM4x; (b) SSM4c1; (c) SSM4c1r; (d) SSM4c3; (e) SSM4c3r; (f) UOM0x; (g) UOM0si. 1 = Ferrihydrite, $Fe_5HO_8{\cdot}4H_2O$; 2 = Fe–Cr–Ni alloy; 3 = Cr_2O_3; 4 = Fe_2O_3; 5 = $NiFe_2O_4$; 6 = metaschoepite, $UO_3{\cdot}1.5H_2O$; 7 = UO_2.

1,703 K), where oxygen was not detected, and the sintering of the UOM0x microsphere (UOM0si, (Figure 8(e))), where the oxygen content was substantially low (7%). In the case of the UOM0si microsphere, the O (7%, low) and U (92%, high) contents (Table 4) may be confirming the formation of hypostoichiometric UO_2 (O/U = 1.13), hence liquid U^0. The actual O/U ratio will be determined in the future through thermogravimetric analysis by re-oxidizing the microsphere [8, 47, 48].

Although EDS analysis is inadequate to determine the exact carbon content [48], in the SSM0r1, SSM4c1r, and SSM4c3r microspheres, it was equal to 2%, 3%, and 2%, respectively (Table 4), which confirms the right choice of calcination condition 1,173 K/air/3 hr to maximize the elimination of the carbon black. These C contents can be reduced by adjusting the calcination condition. C can be solubilized in the α-Fe phase as Fe_3C (see Figure 6(b) and Figures 7(c) and 7(d), respectively) and even in the form of Cr_3C_2 [16, 44, 45]. Increasing the reduction temperature in the SSM4$^+$c3r microsphere seems to have favored the decomposition of Cr_3C_2, the reaction of C with Fe_2O_3 and Cr_2O_3, and the solubilization of the remaining C in the α-Fe phase, in the form of Fe_3C (Figure 8(d), Table 4); in UO_2 microspheres (Figure 8(e), Table 4), the analyzed carbon content was 1%. In summary, this and the other previous results show that it is possible to obtain both Fe, Cr, and Ni oxide microspheres with different degrees of reducibility and UO_2 microspheres with adjustable density, both with predetermined mechanical

Table 4: Chemical composition of the SS and UO_2 microspheres and of the PCERM5 pellet obtained by EDX or EDS analyses.

Codes	CBC* (g)	Elemental composition (%)						
		Fe	Cr	Ni	U	Si	O	C
SSM0x*1	0.0	71	21	6	–	2	–	–
SSM1c3*1	1.5	72	21	5	–	2	–	–
SSM3c3*1	3.0	71	22	5	–	2	–	–
SSM4c1*1	4.5	73	21	5	–	1	–	–
SSM4c2*1	4.5	73	21	5	–	1	–	–
SSM4c3*1	4.5	73	21	5	–	1	–	–
SSM0r1*2	1.5	64	21	5	–	<1	8	2
SSM4c1r*2	4.5	88	7	2	–	<1	–	3
SSM4c2r*2	4.5	ND*3	ND*3	ND*3	–	ND*3	ND*3	ND*3
SSM4c3r*2	4.5	64	18	4	–	<1	12	2
SSM4+c3r*2	4.5	72	18	10	–	–	–	–
UOM0si*2	0.0	–	–	–	92	–	7	1
PCERM5*2	4.5	39	20	5	23	–	13	–

*CBC, Carbon black content; *1EDX or *2EDS analyses; ND*3, not determined.

resistance to compression and a diameter of around 200 μm, thus meeting Holden's postulate [9].

3.2. Holden Approach versus In Situ Micronization Approach in the Fabrication of SS-UO_2 Cermet Pellets. The process developed (Figure 1) enabled the production of two dissimilar materials, that is, two materials characterized by either metallic (SS) and covalent or ionic (UO_2) chemical bonds. Their combination generated the SS-UO_2 pellet. This combination created a metal/ceramic interface with a joint quality, according to the Holden's approach, that depended only on the use of large metallic and ceramic particles (~200 μm) [9]. Other approaches specify that the quality of the joint would depend on the hard or soft nature of the dissimilar particles, as well as on the type of chemical bonds formed. Because of these issues, obtaining good adhesion at the metal/ceramic interface was not trivial and required substantially decreasing the usual large particle size (~45 μm) of the industrial SS particle to favor mass transfer mechanisms, particularly by plastic deformation, especially in the interface region, during the cermet pressing and sintering [6, 16, 27, 40]. In this R&D, this decrease in size was differentiated. The size of the metallic (SS) and ceramic (UO_2) particles was maintained large (~200 μm), but with the SS particle having smaller particles (<5 μm) inside separated by pores (*in situ* micronization approach) [39]. Table 5 (Holden's approach) and Table 6 (*in situ* micronization approach) summarize the manufacturing parameters of the SS-UO_2 cermet pellets obtained, while Figure 9 illustrates the evolution of their macrostructural and microstructural characteristics.

Figures 9(a)–9(a2) and (Table 5) illustrate the macrostructural and microstructural characteristics of the *PCERM1* pellet resulting from the Holden's approach [9]. The use of large ($153 \pm 5/176 \pm 6$ μm), dense (72% TD/99% TD), poor porosity (28%/1%), and rigid ($132.2 \pm 24.7/147.4 \pm 25.0$ MPa) SS/UO_2 particles required a high compaction pressure (980.7 MPa) but still did not produce a green pellet mechanically resistant to handling (Figure 9(a)). This evidenced the incompressible behavior of the fabricated rigid metallic and ceramic microspheres [40, 43]. This behavior did not allow a reasonable plastic deformation for creating contacts (necks) between metal/metal and metal/ceramic microspheres that were strong enough to guarantee the physical integrity of the sintered pellet (Figure 9(a1)). Furthermore, the topological arrangement of the fragmented or deformed SS and UO_2 (see arrow + circle in Figure 9(a2)) particles generated large pores (see the triangle in Figure 9(a2)) that were difficult to eliminate at the sintering temperature used (1,273 K/H_2/0.08 hr and 1,623 K/H_2/2.0 hr), resulting in a fragile and brittle pellet under handling. Note that PCERM1 was made with the SSM0r martensitic microsphere and saw high temperatures and cooling from 1,623 to <1,185 K slow enough to produce an austenitic SS, whose bright grayish-silver color was masked by the high porosity of the pellet. Thus, the rigid inclusion nature of the SSM0r1 microspheres compromised the desired physical integrity of the UO_2 microspheres and made Holden's approach unfeasible [9].

Figures 9(b–b2) to 9(e–e2) and (Table 6) illustrate the macrostructural and microstructural characteristics of the pellets resulting from the *in situ* micronization approach [39]. The porous martensitic microspheres used allowed reducing the compaction pressure from 980.7 to 588.4 MPa. This yielded mechanically resistant green and sintered pellets with preserved UO_2 microsphere physical integrity (see arrows in Figures 9(b1)–9(e1)). *PCERM2* (Figure 9(b)) had poor densification (74% TD). This suggested that the porosity (71%) and the compressive stress (11.0 ± 3.3 MPa) of SSM4c1r (calcined at 873 K/3 hr) required a higher compaction pressure to obtain a green pellet with smaller pores, that is, with more necks between all SS microspheres, and thus inhibit discontinuities at the SS/SS interface (see the triangle in the crack, Figure 9(b1)) in the sintered pellet. Because of this, the elimination of pores by sintering mechanisms was not efficient in PCERM2, even though SSM4c1r microsphere had a particle diameter of 1.6 ± 0.6 μm in its core. We cannot exclude either that the sintering condition used (1,523 K/H_2/0.08 hr and 1,703 K/H_2/2.0 hr) did not facilitate both the solubilization, diffusion, and

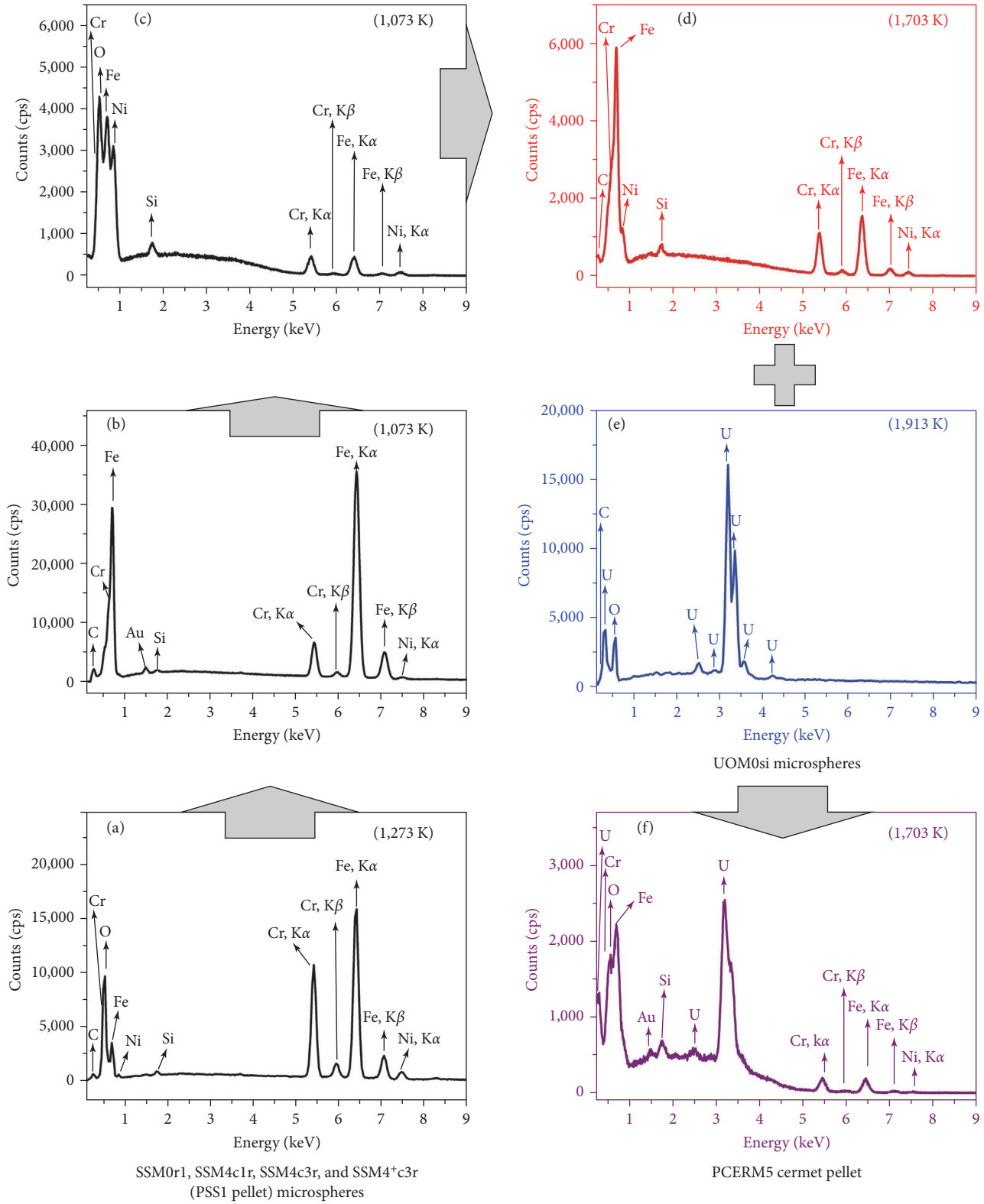

FIGURE 8: EDS spectra illustrating the evolution of the chemical composition of SS and UO_2 microspheres in the oxide–metal conversion process, individually and after obtaining the PCERM5 pellet: (a) SSM0r1; (b) SSM4c1r; (c) SSM4c3r; (d) $SSM4^{+}c3r$ (in the PSS1 pellet); (e) UOM0si; (f) PCERM5.

Table 5: Fabrication parameters of the PCERM1 cermet pellet according to Holden's approach.

Parameters	Mixture of metallic/ceramic microspheres in P1	Cermet pellet (P)
	SSM0r/UOM0si	$\rho_{Pel.}$ (%TD) P1
D_m/D_c (μm)	$153 \pm 5/176 \pm 6$	
D_{Pm}/D_{Pc} (μm)	-/3.5 ± 1.5	
ρ_m/ρ_c (%TD)	72/99	
P_m/P_c (%)	28/1	– **
MR_m/MR_c (MPa)	$132.2 \pm 24.7/147.4 \pm 25.0$	
$P_{comp.}$ (MPa)	980.7	
T_i (K)/t_i (hr)	1,273/0.08	
T_f (K)/t_f (hr)	1,623/2.0	
$D_{Pel.}$ (cm)	–	
$H_{Pel.}$ (cm)	–	
$M_{Pel.}$ (MPa)	–	

*D_m (μm)/D_c (μm), microsphere diameter, where m = metal and c = ceramic; D_{Pm} (μm)/D_{Pc} (μm), particle diameter inside the microsphere; ρ_m (%TD)/ρ_c (% TD), microsphere density; P_m (%)/P_c (%), porosity in the microsphere; MR_m (MPa)/MR_c (MPa), mechanical resistance to compression of the microsphere; $P_{comp.}$ (MPa), pellet compaction pressure; T_i (K)/t_i (h), intermediate sintering temperature/time; T_f (K)/t_f (h), final sintering temperature/time; $D_{Pel.}$ (cm), pellet diameter; $H_{Pel.}$ (cm), pellet height; $M_{Pel.}$ (g), pellet mass; $\rho_{Pel.}$ (%TD), pellet density; P1, PCERM1; and TD, theoretical density; $\rho_{SS\text{-}UO2}$, 9.2 g/cm^3; ρ_{UO2}, 10.97 g/cm^3 [5]; and ρ_{SS}, 7.90 g/cm^3 [6, 10]. **The broken pellet.

Table 6: Fabrication parameters of PCERM2–PCERM5 cermet pellets by the *in situ* micronization approach.

*Parameters	Mixture of metallic/ceramic microspheres in P2, P3, P4, and P5, respectively				Cermet pellets (P) $\rho_{Pel.}$ (%TD)			
	SSM4c1r/UOM0si	SSM4c2r/UOM0si	SSM4c3r/UOM0si	SSM4c3r/UOM0si	P2	P3	P4	P5
D_m/D_c (μm)	$190 \pm 13/176 \pm 6$	$210 \pm 6/176 \pm 6$	$216 \pm 10/176 \pm 6$	$216 \pm 10/176 \pm 6$				
D_{Pm}/D_{Pc} (μm)	$1.6 \pm 0.6/3.5 \pm 1.5$	-/3.5 ± 1.5	$3.1 \pm 1.4/3.5 \pm 1.5$	$3.1 \pm 1.4/3.5 \pm 1.5$				
ρ_m/ρ_c (%TD)	29/99	23/99	17/996	17/99				
P_m/P_c (%)	71/1	77/1	83/1	83/1	74	86	91	93
MR_m/MR_c (MPa)	$11.0 \pm 3.3/147.4 \pm 25.0$	$0.5 \pm 0.2/147.4 \pm 25.0$	$1.3 \pm 0.4/147.4 \pm 25.0$	$1.3 \pm 0.4/147.4 \pm 25.0$				
$P_{comp.}$ (MPa)	588.4	588.4	588.4	588.4				
T_i (K)/t_i (hr)	1,523/0.08	1,523/0.08	1,523/0.08	1,523/2.0				
T_f (K)/t_f (hr)	1,703/2.0	1,703/2.0	1,703/2.0	1,703/4.0				
$D_{Pel.}$ (cm)	1.035	1.052	0.950	0.962				
$H_{Pel.}$ (cm)	0.271	0.257	0.212	0.241				
$M_{Pel.}$ (g)	1.546	1.760	1.258	1.502				

*D_m (μm)/D_c (μm), microsphere diameter, where m = metal and c = ceramic; D_{Pm} (μm)/D_{Pc} (μm), particle diameter inside the microsphere; ρ_m (%TD)/ρ_c (% TD), microsphere density; P_m (%)/P_c (%), porosity in the microsphere; MR_m (MPa)/MR_c (MPa), mechanical resistance to compression of the microsphere; $P_{comp.}$ (MPa), pellet compaction pressure; T_i (K)/t_i (h), intermediate sintering temperature/time; T_f (K)/t_f (h), final sintering temperature/time; $D_{Pel.}$ (cm), pellet diameter; $H_{Pel.}$ (cm), pellet height; $M_{Pel.}$ (g), pellet mass; $\rho_{Pel.}$ (%TD), pellet density; P2, P3, P4, and P5, PCERM2, PCERM3, PCERM4, and PCERM5, respectively; and TD, theoretical density; $\rho_{SS\text{-}UO2}$, 9.2 g/cm^3; ρ_{UO2}, 10.97 g/cm^3 [5]; and ρ_{SS}, 7.90 g/cm^3 [6, 10].

elimination of CO_2 and the local melting and homogenization of the alloy in order to maximize pore elimination. However, it enabled both a flawless SS/UO_2 interface (see the square in Figure 9(b2)) and the complete reduction of Fe_2O_3 and Cr_2O_3 (Figure 9(b2)), resulting in the formation of a ductile austenitic SS as a cermet metal matrix [16, 27, 40, 41, 50, 51]. *PCERM3* (Figure 9(c)) exhibited increased density (86% TD) due to the increased porosity (77%) and the decreased compressive stress (0.5 ± 0.2 MPa) of the SSM4c2r microsphere (previously calcined at 873 K/24 hr). The denser green pellet produced partially inhibited discontinuities at the SS/SS interface (see the triangle in the crack, Figure 9(c1)) and enabled obtain a flawless SS/UO_2 interface (see the square in Figure 9(c2)) in the sintered pellet. However, the increase in the PCERM3 densification hindered the diffusion of H_2 and CO, preventing the complete reduction of Cr_2O_3 (see the circle in Figure 9(c2)), which remained and was identified by EDS analysis (circles in Figures 10(a) and 10(a2)). The elemental map in Figures 10(a–a4) to 10(c–c4) illustrates the evolution of the oxide–metal conversion in PCERM3, PCERM4, and PCERM5 and, additionally, reinforces the absence of discontinuities in the binding of SS at the metal/ceramic interface (see squares in Figures 10(a)–10(c)). *PCERM4* (Figure 9(d)) exhibited a significant increase in density (91% TD) due to the increased porosity (83%) and compressive stress (1.3 ± 0.4 MPa), even with increased

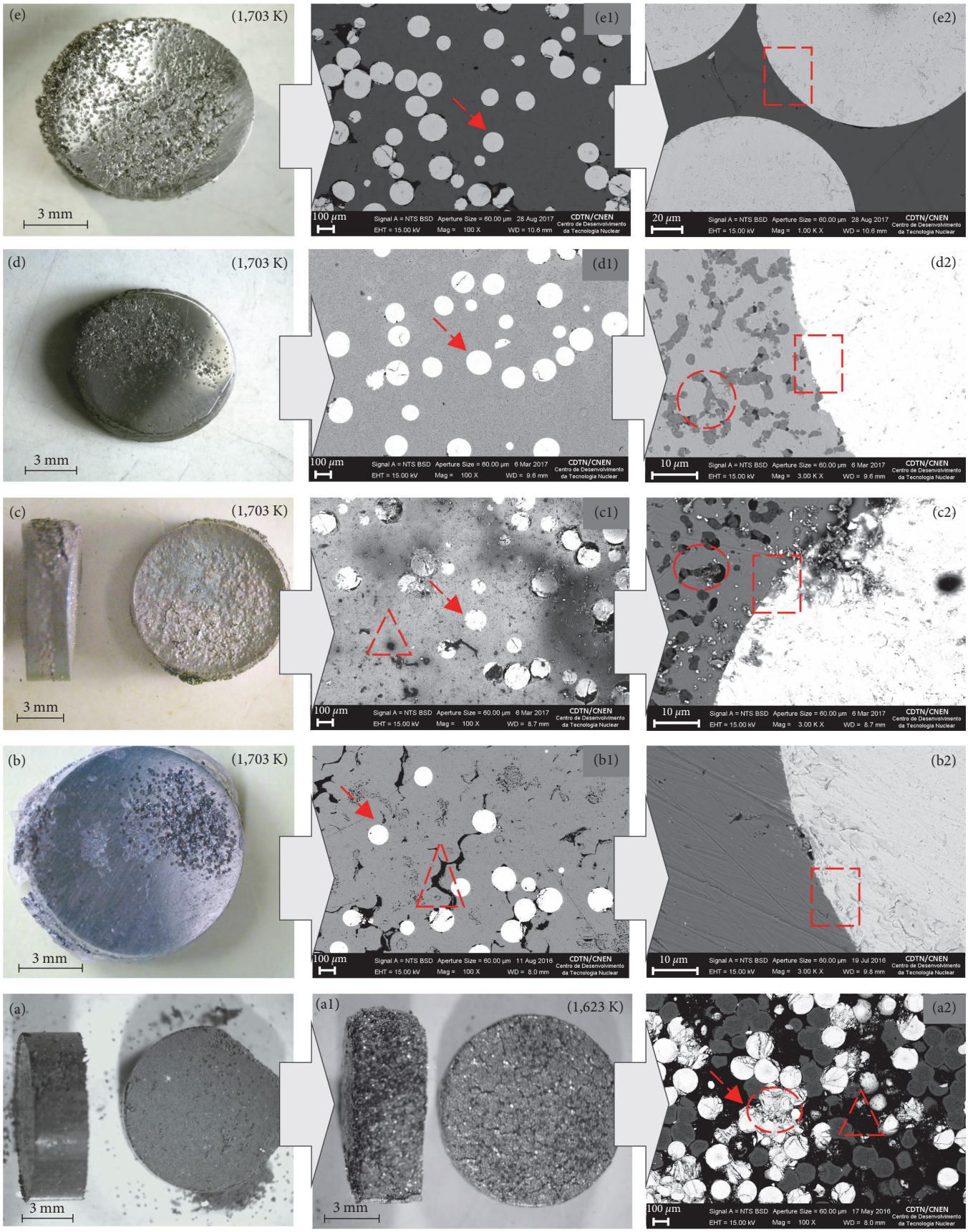

FIGURE 9: Evolution of the macrostructural and microstructural characteristics of the SS-UO_2 cermet pellets according to Holden's approach (a–a2) and the *in situ* micronization approach (b–b2 and e–e2): (a–a2) PCERM1; (b–b2) PCERM2; (c–c2) PCERM3; (d–d2) PCERM4; (e–e2) PCERM5. (a–a2) = green pellets, sintered pellets, and physical integrity of the SS and UO_2 microspheres, respectively; (b–b2), (c–c2), (d–d2), and (e–e2) = sintered pellets, physical integrity of the SS and UO_2 microspheres, and metal/ceramic interface, respectively. Scale bar values: (a2, b1–e1, 100 μm), (b2–d2, 10 μm), and (e2, 20 μm).

particle size ($3.1 \pm 1.4\,\mu$m) inside the SSM4c3r microsphere (previously calcined at 1,173 K/3 hr). The absence of discontinuities in the SS/SS (Figure 9(d1)) and SS-UO_2 (see the square in Figure 9(d2)) interfaces suggests the need for further study to establish the relationship between particle size inside the microsphere, resulting pore arrangement, CO_2 diffusion, and densification [27, 40]. Note that increasing PCERM4 densification also hindered the diffusion of H_2 and CO, preventing the complete reduction of Cr_2O_3 (see circles in Figure 9(d2) and Figures 10(b) and 10(b2)) in the sintered pellet. *PCERM5* (Figure 9(e)) has the same composition as PCERM4 (Figure 9(d)), differing only in the sintering condition, which was changed from 1,523 K/H2/0.08 hr and 1,703 K/H2/2.0 hr to 1,523 K/H2/2.0 hr and 1,703 K/H2/4.0 hr. This was enough to increase the density from 91% to 93% TD, completely convert Cr_2O_3 (see Figure 9(e1) and Figures 10(c) and 10(c2)), eliminate discontinuities in the SS/SS interface, and produce a flawless SS/UO_2 interface (see the square in Figure 9(e2)) in the sintered pellet. Figure 8(f) shows the effect of the austenitic SS (Figure 8(d)) overlapping the UO_2 peaks (Figure 8(e)) and suggesting the complete encapsulation of the UO_2 microsphere in PCERM5 (Figure 8(f)) [8]. The absence of discontinuity at the SS/UO_2 interface suggests that the SS liquid phase formed *in situ* adequately wetted the surface of the UO_2 microsphere and caused a strong interaction between the two dissimilar materials. However, the metallic/covalent and ionic bond interaction across the metal/ceramic interface is still not fully understood [27]. Because of this, the *ab initio* calculations tool [27, 52] has been used to predict and study the nature of these bonds. An example of this study has been reported for the Ni(001)/c-ZrO_2 interface, where the occurrence of Ni–Zr hybridization and ionic Ni–O bonding was predicted [27]. Anyway, the flawless SS/UO_2 interface evidences a strong bonding of the ductile SS with the surface of the UO_2 microsphere. This favors the dissipation of most thermal stresses, increases the conductivity of the heat generated in the UO_2 microsphere, and enhances the hardness of the cermet [27, 51]. Regarding the cermet pellet hardness, PCERM5 (Figure 9(e)) was the only one to show high wear resistance during ceramographic preparation. However, it is noted that PCERM5 (Figure 9(e1)) does not exhibit other desired characteristics [9]: UO_2 microsphere homogeneous distribution, high UO_2 volume fraction, and null connection between UO_2 microspheres. The idea for solving these three bottlenecks came from the microstructural analysis of the PSS1 pellet (Figure 11).

Figure 11 shows the effect of compaction pressure on the compressibility of the soft $SSM4^+c3r$ martensitic microspheres (Figure 11(a)) and on the densification of the PSS1 pellet (Figure 11(a1)). The compaction pressure had been insufficient to eliminate discontinuities at the SS/SS interface (see the circle in Figure 11(a2)), even though the pellet was sintered at 1,523 K/H_2/2.0 hr and 1,703 K/H_2/4.0 hr. Figure 11(a3) suggests that some microspheres did not micronize *in situ*, but were only compressed, maintaining a spheroid shape (see arrow in Figure 11(a3)). Figure 11(a4) illustrates the homogeneous distribution of Fe, Cr, and Ni in the formed austenitic SS.

Figure 11(a3) inspired us to develop the concept of SS-UO_2 cermet microspheres, that is, UO_2 microspheres coated with a coherent SS layer, aiming to solve the three mentioned bottlenecks in the continuity of this R&D. The SS-UO_2 cermet microspheres manufactured are shown in Figures 12(a)–12(a6). The usage of a high volume fraction of SS (or Fe, Cr, and Ni oxide)-UO_2 cermet microspheres and a low volume fraction of porous SS (or Fe, Cr, and Ni oxide) microspheres can solve those three referred bottlenecks. As an additional result, this showed us two perspectives on the evolution of the developed nonconventional powder metallurgy process. These two perspectives are already being implemented in the fabrication of both SS-UO_2 cermet microspheres and magnetic porous NdFeB microspheres in our laboratory. The optimization of the SS-UO_2 cermet microsphere (Figures 12(a)–12(a6)) manufacturing conditions is already well advanced. However, additional work is needed to maximize the SS layer thickness to around 30 μm [9] and, thus, obtain optimal SS-UO_2 cermet pellets (more details in the Supplementary Material). Porous NdFeB microspheres are already being manufactured in order to produce high-performance rare earth magnets. The preliminary results are very promising.

3.3. Oxide–Metal Reduction Mechanisms. Figure 5 shows the high porosity of the SSM4c1r microsphere. It gives a great example of the solid–gas reaction mechanism [53]. According to this mechanism, the reaction zone occurs first in the outermost layer of the micro- and/or the nanoparticles that make up the microsphere and then moves into these micro- and/or nanoparticles, leaving behind completely converted and inert material, or rather, the reaction products [54], in this case, the Fe–Cr–Ni alloy + H_2O and/or CO_2. A tiny unreacted nucleus of metal oxide (Fe_2O_3 and Cr_2O_3) can often remain [53]. In general, the complete reduction of the oxide depends on [53, 55–57]: an increasing temperature (Fe_2O_3, ≥1,243 K [58]; NiO, >1,173 K [54] and Cr_2O_3, >1,300 K [59]), the reducing atmosphere composition (H_2 and/or CO, ultrapure or containing N_2 or Ar or H_2O), and the material properties, for example, those related to the nanostructuring of the Fe_2O_3, Cr_2O_3, and NiO particles and the presence of pores in the microsphere produced.

According to Puigdollers et al. [55], the reducibility of an oxide depends on the generation of oxygen vacancies, which can be created via: doping of the oxide network, in this case, those of Fe_2O_3, Cr_2O_3, and NiO; nanostructuring of the material; and formation of a metal/oxide interface. In this work, considering the SS microspheres containing or not carbon black, the ≡C (meaning carbon on the surface of the carbon black and/or the cross-linked PVA nanoparticles)/oxide interface cannot be excluded. This generation of vacancies would measure the tendency of the oxide to lose or donate oxygen to an "adsorbent species" [26], leading to a progressive change in the surface composition of this oxide from M_nO_m to M_nO_{m-x}, that is, reducing it. In the present work, this adsorbent species can be initially represented by the surfaces of both Mo^0 or Pt^0 (crucible materials) and/or ≡C and, later, of both the metal (Fe^0 and/or Ni^0 and/or Cr^0) and/or the Fe–Cr–Ni alloy formed, without excluding the

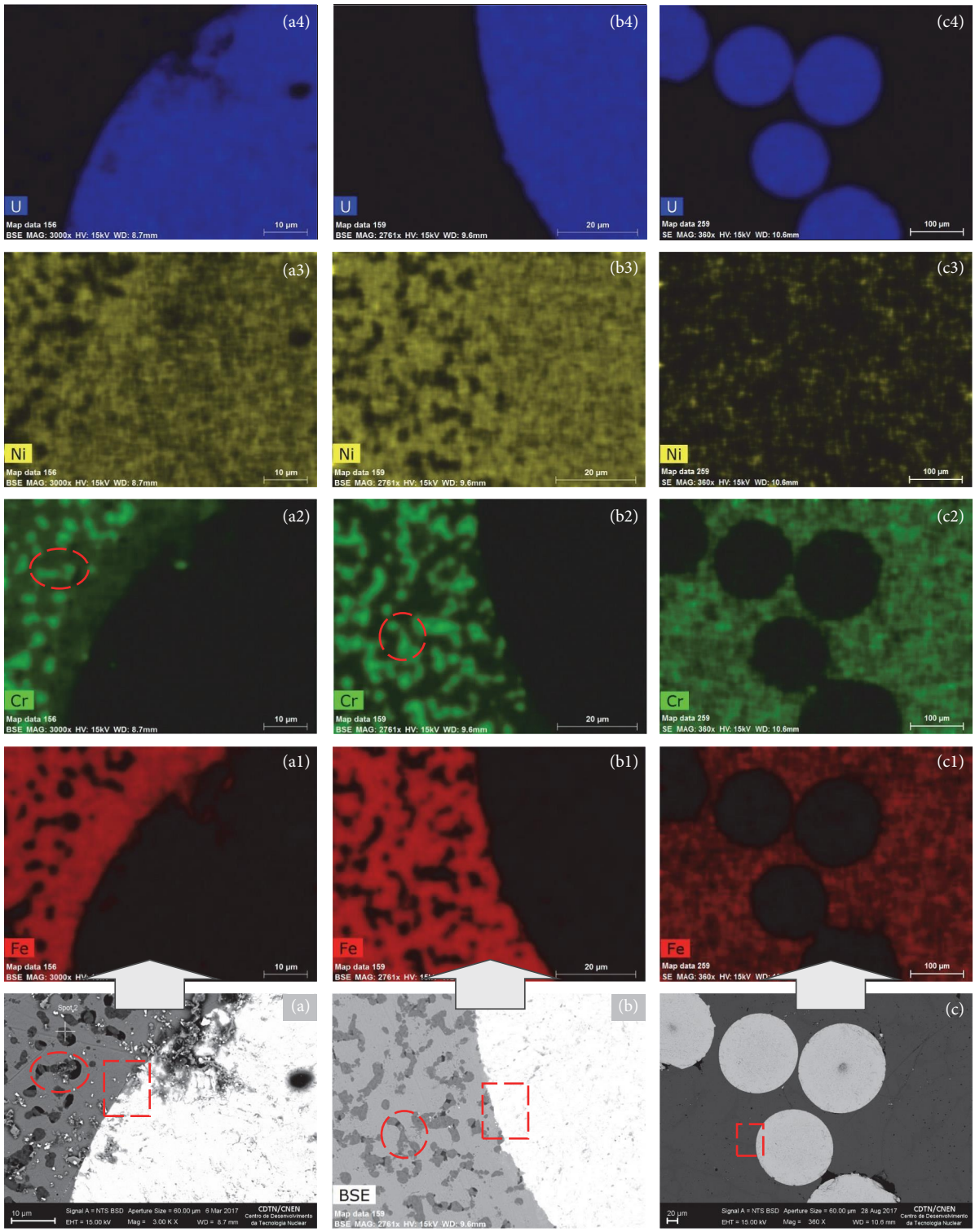

FIGURE 10: Elemental map showing the evolution of the oxide–metal conversion in the SS-UO_2 cermet pellets and reinforcing the absence of discontinuities in the SS binding at the metal/ceramic interface: (a, a1–a4) PCERM3; (b, b1–b4) PCERM4; and (c, c1–c4) PCERM5. (a, a1–a4), (b, b1–b4), and (c, c1–c4) = metal/ceramic interface (a–c), Fe in the Fe–Cr–Ni alloy, red (a1, b1, c1), Cr in the Fe–Cr–Ni alloy, green (a2, b2, c2), Ni in the Fe–Cr–Ni alloy, yellow (a3, b3, c3), and U in the UO_2 microsphere, blue (a4, b4, c4). Scale bar values: (a–a4, 10 μm), (b1–b4, 20 μm), (c, 20 μm), and (c1–c4, 100 μm).

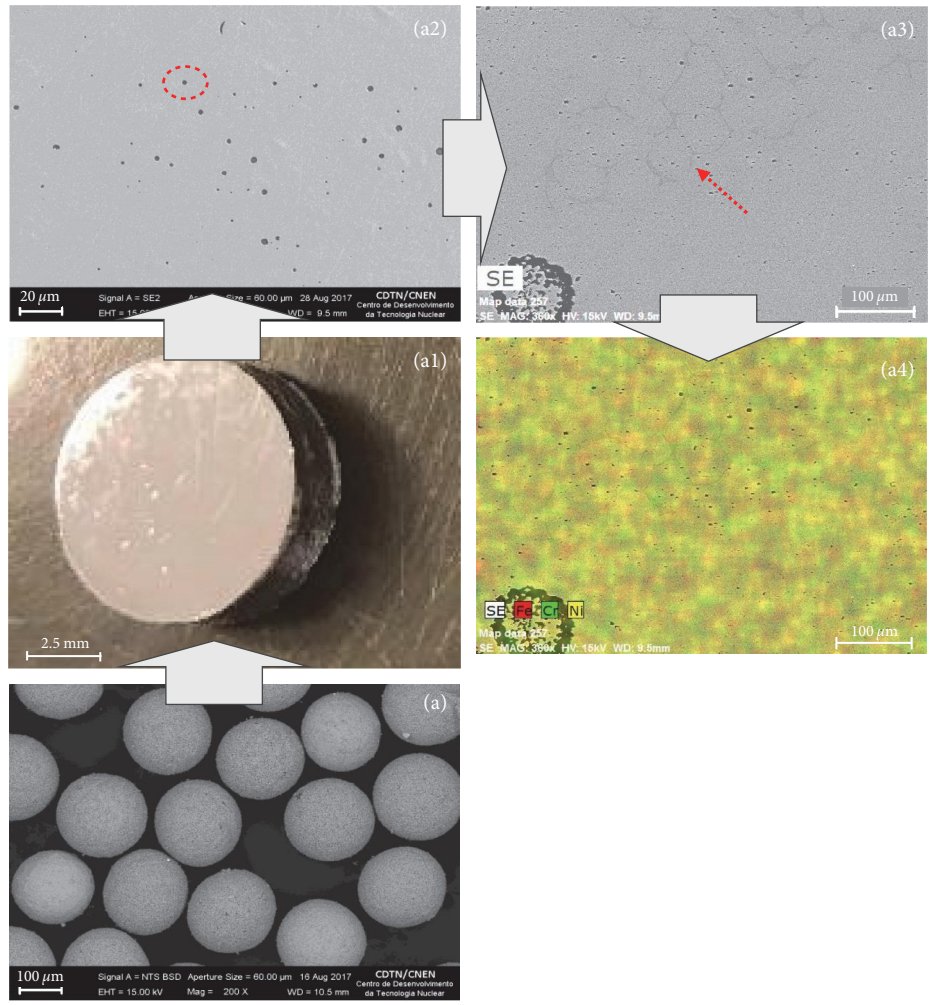

FIGURE 11: Effect of compaction pressure on the compressibility of the martensitic soft SSM4^{+}c3r microspheres and on the densification of the PSS1 pellet: (a) SSM4^{+}c3r microspheres; (a1) PSS1 sintered pellet; (a2) PSS1 polished surface; (a3) visualization of the compressed soft SSM4^{+}c3r microspheres; and (a4) PSS1 elemental map (red = Fe, green = Cr, and yellow = Ni). Scale bar values: (a, 100 μm), (a2, 20 μm), and (a3 and a4, 100 μm).

"adsorbent role" of the reducing atmosphere (H_2 and CO). Helali et al. [60] represent the mechanism for creating a vacancy by Equation (1).

$$MO_x = MO_{x-1} + \frac{1}{2}O_2 \quad (1)$$

The valences of the elements in the Fe_2O_3, Cr_2O_3, and NiO oxides play an important role in the reduction of the SSM0r microsphere, for instance [55]. The presence of Ni^{2+} and Cr^{3+} has a significant effect on the reducibility of Fe_2O_3. The substitution of Fe^{3+} with Cr^{3+} in the Fe^{3+} crystal lattice creates size effects or, at most, a shift of the frontier orbitals with a consequent change in the strength of the Fe^{3+}–O and Cr^{3+}–O bonds [55]. In the case of Ni^{2+}, when Ni^{2+} replaces Fe^{3+} in the crystal lattice, a charge imbalance is created that needs to be compensated by other types of defects in the crystal lattice, an oxygen vacancy close to Ni^{2+}, for example [55]. Thus, acting as dopants, Cr^{3+} and Ni^{2+} contribute to the release of oxygen from the Fe_2O_3 network, progressively reducing it ($Fe_2O_3 \longrightarrow Fe_3O_4 \longrightarrow FeO \longrightarrow Fe^0$ [58]) [55].

In the present work, metal (and/or ≡C)/oxide interfaces [55] were successfully formed between Mo^0/Fe_2O_3, Pt^0/Fe_2O_3, Fe^0/Fe_2O_3, Fe^0/Cr_2O_3, Fe^0/NiO, ≡C/Fe_2O_3, etc. They were responsible for generating and releasing a large quantity of chemical energy in the form of heat during reduction [41, 61]. As evidenced by the case of microsphere SSM4c1 (Figure 7(c) and 2(f)), the preservation of the ≡C/oxide interface was crucial for the formation of the Fe–Cr–Ni alloy at low temperature (873/air/3/2.3/Pt; Table S2). Regarding nanostructuring [55], it is worth noting that the size of the nanoparticles in the xerogel microspheres was only determined for UOM0x (7.5 nm), but Santos et al. [21] show that in Fe-containing microspheres, such as SSM0x-SSM4^{+}x microspheres, the size is predominantly below 20 nm. Because of this, the Fe_2O_3 and/or Cr_2O_3 and/or NiO nanoparticles in the

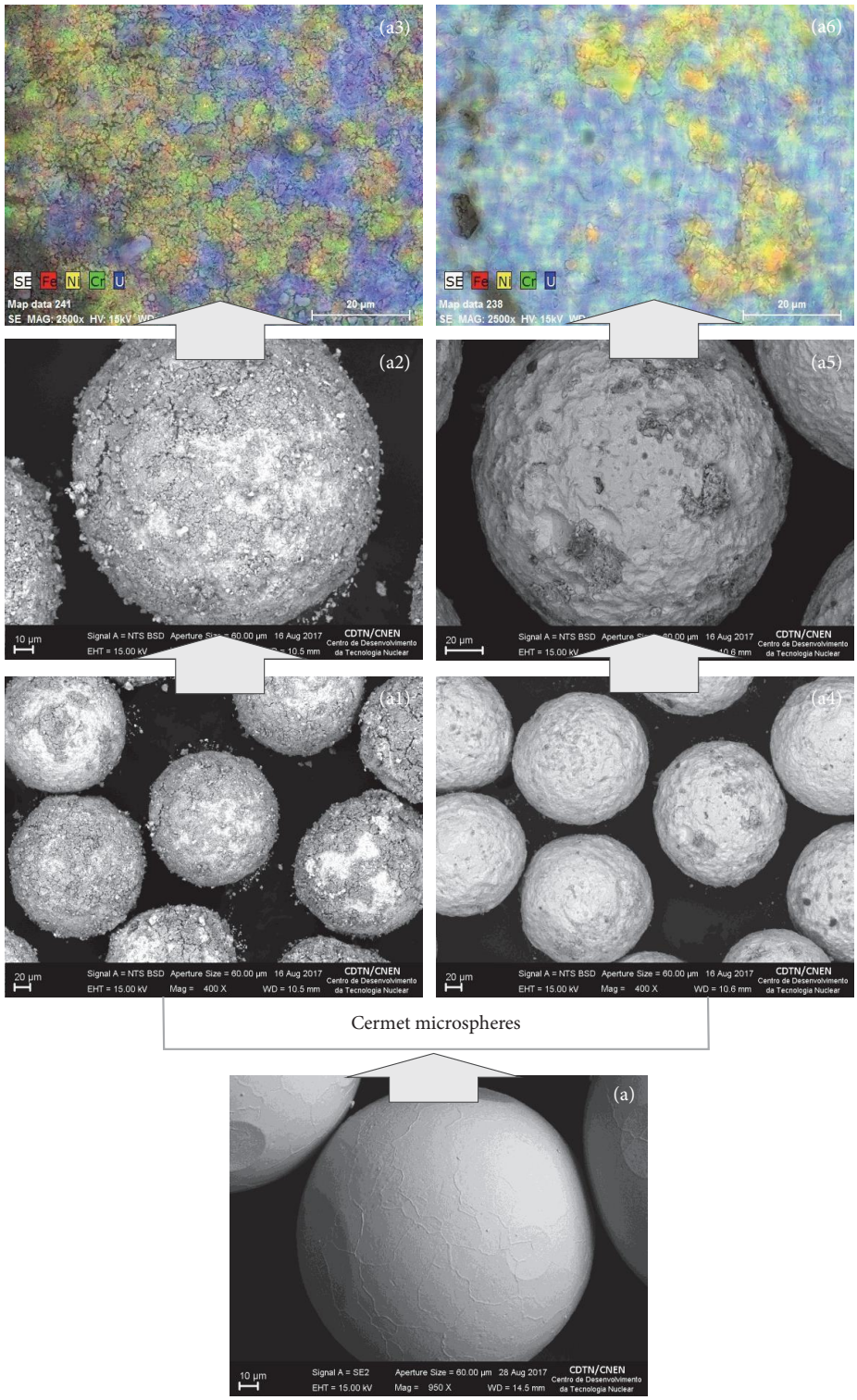

FIGURE 12: Creation of Fe, Cr, and Ni oxyhydroxide multilayers on the surface of UO_2 microspheres aiming at the fabrication of cermet SS-UO_2 microspheres: (a) UOM0si; (a1) and (a4) SS-UO_2 cermet microspheres with 12 and 15 coherent layers of Fe, Cr, and Ni oxyhydroxides, respectively; (a2) and (a5) magnification of (a1) and (a4), respectively; and (a3) and (a6) elemental map of (a2) and (a5), respectively. (red = Fe, green = Cr, yellow = Ni, and blue = U). Scale bar values: (a, 10 μm), (a1, a2, a4, and a6, 20 μm), and (a3 and a5, 10 μm).

SSM0x microsphere, for example, have oxygen ions in poorly coordinated sites on their surfaces. As a result of this low coordination, these sites start to have high chemical reactivity, which facilitates the removal of the oxygen through the reaction with carbon and metal (due to the aforementioned metal (and/or ≡C)/oxide interfaces) and/or with H_2 [26, 41, 55–57, 61]. These reactions can be represented by Equations (2–5) [55, 61, 62].

$$M^*/MO_x = M^*O_x + M \quad (2)$$

$$\equiv C/MO_x = MO_{x-1} + CO \quad (3)$$

$$MO_x + CO = MO_{x-1} + CO_2 \quad (4)$$

$$MO_x + H_2 = MO_{x-1} + H_2O \quad (5)$$

In Reaction (2), metal M^* has a higher affinity for oxygen than metal M [61]. In Reactions (4) and (5), the by-products, CO_2 and H_2O, were eliminated from the microspheres by diffusion into the remaining pores and grain boundaries [55, 63]. Thus, the first metallic clusters (Fe^0 and/or Ni^0 and/or Cr^0) formed at the oxide/metal (Mo or Pt) or the ≡C/oxide interfaces progressively formed interfaces with the remaining oxides (Cr_2O_{3-x} and/or Fe_2O_{3-x} and/or NiO_{1-x}), where the oxide reactivity was significantly increased and oxygen could be easily removed [41, 55, 61, 62]. These metallic clusters are formed by diffusion of the metallic cations in the crystal lattice [41, 63].

4. Conclusion

The nonconventional powder metallurgy process developed here can solve the bottlenecks found in the manufacture of SS-UO_2 cermet pellets because it allows obtaining SS, UO_2, and SS-UO_2 cermet microspheres with customized characteristics. Hard ($153 \pm 5\,\mu$m; 132.2 ± 24.7 MPa; 72% TD) and soft ($216 \pm 10\,\mu$m; 1.3 ± 0.4 MPa; 17% TD) SS microspheres with partial oxide–metal conversion have been obtained; full conversion is quite possible. Hard ($176 \pm 6\,\mu$m; 147.4 ± 25.0 MPa; 99% TD) UO_2 microspheres have been fabricated. Soft porous SS microspheres containing mainly Fe–Cr–Ni alloy did not micronize properly *in situ*, but their high compressibility favors the compaction of the green SS-UO_2 cermet pellet. This enabled the obtainment of sintered SS-UO_2 cermet pellets with high densities (93% TD), excellent metal–ceramic interaction, and maintenance of the physical integrity of the UO_2 microspheres. The SS-UO_2 cermet microspheres under development will enable obtaining SS-UO_2 cermet pellets with a volume fraction greater than 42 vol% UO_2, with a homogeneous distribution of UO_2 microspheres, and with null connection between them. The nonconventional powder metallurgy process developed has great potential to be used in the manufacture of porous NdFeB microspheres, a raw material with interesting characteristics useful in the manufacture of high-performance rare earth magnets.

Data Availability

The data used to support the findings of this study are included in the article. Additional information can be obtained directly from the corresponding author.

Conflicts of Interest

The authors declare that they have no conflicts of interest.

Acknowledgments

We are grateful for the material and financial support from Conselho Nacional de Desenvolvimento Científico e Tecnológico–CNPq (process no.: 310127/2009-2; Public Notice/Call: Productivity in Technological Development and Innovative Extension-DT 2009). SEM/EDS analyses were done at the CDTN Microscopy Center by Tercio Assunção Pedrosa and Sérgio Carneiro dos Reis and the analyses of mechanical resistance to compression of the SS and UO_2 microspheres were done at SEMAV/CDTN by Jefferson José Vilela and Jonnas Peressinotto.

Supplementary Materials

Table S1: CBC and drying parameters of the hydrogel microspheres. Table S2: Sintering (si) and/or calcination (c) and/or reduction (r) sequential thermal treatment (STT) parameters (T(K)/atm./DT(hr)/HR(K/min)/CM) of the xerogel microspheres. Table S3: SS-UO_2 and SS pellet pressing parameters. Table S4: Sequential thermal treatment (STT) parameters of the SS-UO_2 cermet and SS pellets. Ni content adjustment experiment in SSM4h microspheres; apparatus used in the production of SS and UO_2 microspheres and the pressing and sintering of SS-UO_2 cermet and SS pellets; XRD analysis details; attesting the technical feasibility of manufacturing SS-UO_2 cermet microspheres. (*Supplementary Materials*)

References

[1] S. Suman, "Hybrid nuclear-renewable energy systems: a review," *Journal of Cleaner Production*, vol. 181, pp. 166–177, 2018.

[2] K. L. Murty and I. Charit, "Structural materials for Gen-IV nuclear reactors: challenges and opportunities," *Journal of Nuclear Materials*, vol. 383, no. 1-2, pp. 189–195, 2008.

[3] G. S. Was, D. Petti, S. Ukai, and S. Zinkle, "Materials for future nuclear energy systems," *Journal of Nuclear Materials*, vol. 527, Article ID 151837, 2019.

[4] D.-J. Kim, Y. W. Rhee, J. H. Kim et al., "Fabrication of microcell UO_2–Mo pellet with enhanced thermal conductivity," *Journal of Nuclear Materials*, vol. 462, pp. 289–295, 2015.

[5] S. C. Finkeldei, J. O. Kiggans, R. D. Hunt, A. T. Nelson, and K. A. Terrani, "Fabrication of UO_2-Mo composite fuel with enhanced thermal conductivity from sol-gel feedstock," *Journal of Nuclear Materials*, vol. 520, pp. 56–64, 2019.

[6] A. Fernández, R. J. M. Konings, and J. Somers, "Design and fabrication of specific ceramic–metallic fuels and targets," *Journal of Nuclear Materials*, vol. 319, pp. 44–50, 2003.

[7] S. Mishra, P. S. Kutty, T. R. G. Kutty, S. Das, G. K. Dey, and A. Kumar, "Cermet fuel for fast reactor—fabrication and characterization," *Journal of Nuclear Materials*, vol. 442, no. 1–3, pp. 400–407, 2013.

[8] W. F. Cureton, J. Zillinger, J. Rosales, R. P. Wilkerson, M. Lang, and M. Barnes, "Microstructural evolution of Mo-UO_2 cermets under high temperature hydrogen environments," *Journal of Nuclear Materials*, vol. 538, Article ID 152297, 2020.

[9] R. B. Holden, *Ceramic Fuel Elements*, Gordon and Breach, New York, (MonographSeries on Metallurgy in Nuclear Technology), 1966.

[10] G. Arthur and J. A. Coulson, "Physical properties of uranium dioxide-stainless steel cermets," *Journal of Nuclear Materials*, vol. 13, no. 2, pp. 242–253, 1964.

[11] D. E. Burkes, D. M. Wachs, J. E. Werner, and S. D. Howe, "An Overview of Current and Past W-UO_2 CERMET Fuel Fabrication Technology," in *Proceedings of Space Nuclear Conference 2007*, pp. 207–216, Boston, Massachusetts, INL, June 2007.

[12] D. S. Tucker, "CERMETS for use in nuclear thermal propulsion," in *Advances in Composite Materials Development*, D. Lucan, Ed., pp. 11–24, IntechOpen, 2019.

[13] OECD, *State-of-the-Art Report on Innovative Fuels for Advanced Nuclear Systems*, pp. 1–195, OECD Publishing, Paris, 2015.

[14] R. D. Hunt, R. R. Hickman, J. L. Ladd-Lively, K. K. Anderson, R. T. Collins, and J. L. Collins, "Production of small uranium dioxide microspheres for cermet nuclear fuel using the internal gelation process," *Annals of Nuclear Energy*, vol. 69, pp. 139–143, 2014.

[15] C. Huber, H. Sepehri-Amin, M. Goertler et al., "Coercivity enhancement of selective laser sintered NdFeB magnets by grain boundary infiltration," *Acta Materialia*, vol. 172, pp. 66–71, 2019.

[16] B. AL-Mangour, "Powder metallurgy of stainless steel: state-of-the art, challenges, and development," in *Stainless Steel*, pp. 37–80, Nova Science Publishers, Inc., 2015.

[17] H. Irrinki, J. S. D. Jangam, S. Pasebani et al., "Effects of particle characteristics on the microstructure and mechanical properties of 17-4 PH stainless steel fabricated by laser-powder bed fusion," *Powder Technology*, vol. 331, pp. 192–203, 2018.

[18] G. Vasudevamurthy and T. W. Knight, "Effect of system parameters on size distribution of 304 stainless steel particles produced by electrical discharge mechanism," *Materials Letters*, vol. 61, no. 27, pp. 4872–4874, 2007.

[19] I. Bica, "On the mechanisms of iron microspheres formation in argon plasma jet," *Journal of Magnetism and Magnetic Materials*, vol. 257, no. 1, pp. 119–125, 2003.

[20] C. Ganguly and U. Basak, "Fabrication of high density UO_2 fuel pellets involving sol–gel microsphere pelletisation and low temperature sintering," *Journal of Nuclear Materials*, vol. 178, no. 2-3, pp. 179–183, 1991.

[21] A. Santos, F. W. F. de Oliveira, F. H. A. Silva et al., "Synthesis and characterization of iron-PVA hydrogel microspheres and their use in the arsenic (V) removal from aqueous solution," *Chemical Engineering Journal*, vol. 210, pp. 432–443, 2012.

[22] C. L. L. de Faria Jr., T. K. R. de Oliveira, V. L. dos Santos et al., "Usage of the sol–gel process on the fabrication of macroporous adsorbent activated-gamma alumina spheres," *Microporous and Mesoporous Materials*, vol. 120, no. 3, pp. 228–238, 2009.

[23] M. Z. Mehrizi, J. Abdi, M. Rezakazemi, and E. Salehi, "A review on recent advances in hollow spheres for hydrogen storage," *International Journal of Hydrogen Energy*, vol. 45, no. 35, pp. 17583–17604, 2020.

[24] L. Wu, Y. Li, Z. Fu, and B.-L. Su, "Hierarchically structured porous materials: synthesis strategies and applications in energy storage," *National Science Review*, vol. 7, no. 11, pp. 1667–1701, 2020.

[25] Y. Xie, D. Kocaefe, C. Chen, and Y. Kocaefe, "Review of research on template methods in preparation of nanomaterials," *Journal of Nanomaterials*, vol. 2016, Article ID 2302595, 10 pages, 2016.

[26] F. W. F. de Oliveira, S. C. dos Reis, L. S. Ribeiro et al., "Fluorine adsorption on floating iron nanoparticles confined to gigaporous structure of large adsorbent water spheres," *Environmental Technology & Innovation*, vol. 24, Article ID 101995, 2021.

[27] J. S. Moya, S. Lopez-Esteban, and C. Pecharromán, "The challenge of ceramic/metal microcomposites and nanocomposites," *Progress in Materials Science*, vol. 52, no. 7, pp. 1017–1090, 2007.

[28] F. Arduini, S. Cinti, V. Mazzaracchio, V. Scognamiglio, A. Amine, and D. Moscone, "Carbon black as an outstanding and affordable nanomaterial for electrochemical (bio)sensor design," *Biosensors and Bioelectronics*, vol. 156, Article ID 112033, 2020.

[29] J. Xia, G. He, L. Zhang, X. Sun, and X. Wang, "Hydrogenation of nitrophenols catalyzed by carbon black-supported nickel nanoparticles under mild conditions," *Applied Catalysis B: Environmental*, vol. 180, pp. 408–415, 2016.

[30] L. Shi and Q. Han, "Molecular dynamics study of deformation mechanisms of poly(vinyl alcohol) hydrogel," *Molecular Simulation*, vol. 44, no. 17, pp. 1363–1370, 2018.

[31] H. Liao, Y. Liu, Q. Wang, and W. Duan, "Structure and properties of porous poly(vinyl alcohol) hydrogel beads prepared through a physical–chemical crosslinking method," *Journal of Applied Polymer Science*, vol. 135, no. 26, Article ID 46402, 2018.

[32] S. Komiya, E. Otsuka, Y. Hirashima, and A. Suzuki, "Salt effects on formation of microcrystallites in poly(vinyl alcohol) gels prepared by cast-drying method," *Progress in Natural Science: Materials International*, vol. 21, no. 5, pp. 375–379, 2011.

[33] L. Y. Ng, A. W. Mohammad, C. P. Leo, and N. Hilal, "Polymeric membranes incorporated with metal/metal oxide nanoparticles: a comprehensive review," *Desalination*, vol. 308, pp. 15–33, 2013.

[34] Z. Shang, M. M. Hossain, R. Wycisk, and P. N. Pintauro, "Poly(phenylene sulfonic acid)-expanded polytetrafluoroethylene composite membrane for low relative humidity operation in hydrogen fuel cells," *Journal of Power Sources*, vol. 535, Article ID 231375, 2022.

[35] N. J. Tro, *Chemistry: A Molecular Approach*, Pearson, Boston, 4th edition, 2017.

[36] K. Mohammad and N. Saheb, "Molecular level mixing: an approach for synthesis of homogenous hybrid ceramic nanocomposite powders," *Powder Technology*, vol. 291, pp. 121–130, 2016.

[37] B. A. Rozenberg and R. Tenne, "Polymer-assisted fabrication of nanoparticles and nanocomposites," *Progress in Polymer Science*, vol. 33, no. 1, pp. 40–112, 2008.

[38] S. F. Costa, *Illustrated Introduction to Statistics*, Editora Harbra Ltd, São Paulo, Brazil, 3rd edition, 1998.

[39] K. R. Vandana, Y. Prasanna Raju, V. Harini Chowdary, M. Sushma, and N. Vijay Kumar, "An overview on *in situ* micronization technique—an emerging novel concept in advanced drug delivery," *Saudi Pharmaceutical Journal*, vol. 22, no. 4, pp. 283–289, 2014.

[40] W. David Kingery, H. K. Bowen, and D. R. Uhlmann, *Introduction to Ceramics*, John Wiley & Sons, New York, 2nd edition, 1960.

[41] P. Jena and A. W. Castleman Jr., "Clusters: a bridge across the disciplines of physics and chemistry," *Proceedings of the National Academy of Sciences*, vol. 103, no. 28, pp. 10560–10569, 2006.

[42] O. V. Khoruzhii, S. Y. Kourtchatov, and V. V. Likhanskii, "New model of equiaxed grain growth in irradiated UO_2," *Journal of Nuclear Materials*, vol. 265, no. 1-2, pp. 112–116, 1999.

[43] G. W. Scherera, "Sintering with rigid inclusions," *Journal of The American Ceramic Society*, vol. 70, no. 10, pp. 719–725, 1987.

[44] E. S. Davenport and E. C. Bain, "Transformation of austenite at constant subcritical temperatures," *Metallurgical and Materials Transactions B*, vol. 1, pp. 3503–3530, 1970.

[45] V. Chiaverini, *Heat Treatments of Ferrous Alloys*, Associação Brasileira de Metalurgia-ABM, São Paulo, Brazil, 2nd edition, 1987.

[46] W. R. Bower, K. Morris, F. R. Livens et al., "Metaschoepite dissolution in sediment column systems—implications for uranium speciation and transport," *Environmental Science & Technology*, vol. 53, no. 16, pp. 9915–9925, 2019.

[47] N. P. Fairbanks and J. A. McGurty, "Method for producing stoichiometric uranium dioxide compositions," US Patent 3,573,036, 1971.

[48] E. K. Papynov, O. O. Shichalin, A. Y. Mironenko et al., "Synthesis of high-density pellets of uranium dioxide by spark plasma sintering in dies of different types," *Radiochemistry*, vol. 60, pp. 362–370, 2018.

[49] S. J. B. Reed, *Electron Microprobe Analysis and Scanning Electron Microscopy in Geology*, Cambridge University Press, New York, 2nd edition, 2005.

[50] K. Saeidi, X. Gao, Y. Zhong, and Z. J. Shen, "Hardened austenite steel with columnar sub-grain structure formed by laser melting," *Materials Science and Engineering: A*, vol. 625, pp. 221–229, 2015.

[51] Y. Wang, K. Zhang, Z. Guo, N. Chen, and Y. Rong, "A new effect of retained austenite on ductility enhancement in high strength bainitic steel," *Materials Science and Engineering: A*, vol. 552, pp. 288–294, 2012.

[52] W. A. Goddard III and L. B. Harding, "The description of chemical bonding from ab initio calculations," *Annual Review of Physical Chemistry*, vol. 29, pp. 363–396, 1978.

[53] O. Levenspiel, *Chemical Reaction Engineering*, John Wiley & Sons, 2nd edition, 1972.

[54] K. V. Manukyan, A. G. Avetisyan, C. E. Shuck et al., "Nickel oxide reduction by hydrogen: kinetics and structural transformations," *The Journal of Physical Chemistry C*, vol. 119, no. 28, pp. 16131–16138, 2015.

[55] A. R. Puigdollers, P. Schlexer, S. Tosoni, and G. Pacchioni, "Increasing oxide reducibility: the role of metal/oxide interfaces in the formation of oxygen vacancies," *ACS Catalysis*, vol. 7, no. 10, pp. 6493–6513, 2017.

[56] N. Zhang, T. Zhou, J. Ge et al., "High-density planar-like Fe_2N_6 structure catalyzes efficient oxygen reduction," *Matter*, vol. 3, no. 2, pp. 509–521, 2020.

[57] T. Zhou, H. Shan, H. Yu et al., "Nanopore confinement of electrocatalysts optimizing triple transport for an ultrahigh-power-density zinc–air fuel cell with robust stability," *Advanced Materials*, vol. 32, no. 47, Article ID 2003251, 2020.

[58] J. Zieliński, I. Zglinicka, L. Znak, and Z. Kaszkur, "Reduction of Fe_2O_3 with hydrogen," *Applied Catalysis A: General*, vol. 381, no. 1-2, pp. 191–196, 2010.

[59] W. F. Chu and A. Rahmel, "The kinetics of the reduction of chromium oxide by hydrogen," *Metallurgical Transactions B*, vol. 10, pp. 401–407, 1979.

[60] Z. Helali, A. Jedidi, O. A. Syzgantseva, M. Calatayud, and C. Minot, "Scaling reducibility of metal oxides," *Theoretical Chemistry Accounts*, vol. 136, Article ID 100, 2017.

[61] V. M. Orlov and M. V. Kryzhanov, "Magnesium-thermic reduction of tantalum oxide by self-propagating high-temperature synthesis," *Russian Metallurgy (Metally)*, vol. 2010, pp. 384–388, 2010.

[62] R. A. Mackay and W. Henderson, *Introduction to Modern Inorganic Chemistry*, Taylor & Francis, London, 6th edition, 2002.

[63] R. L. Coble, "Sintering crystalline solids. II. experimental test of diffusion models in powder compacts," *Journal of Applied Physics*, vol. 32, no. 5, Article ID 793, 1961.